Project Acronym:

SOUNDPET (ENTERPRISES/0918/0008)

MRI-guided Focused ultraSOUND system for cancer in PETs (dogs and cats)

Deliverable number: 6.1

Title: MRI compatibility of the transducer and robotic system

Prepared by:

Leonidas Georgiou (GOC)
Natalie Panayiotou (GOC)
Theodora Christodoulou (GOC)
Cleanthis Ioannides (GOC)
Christakis Damianou (CUT)
Nikolas Evripidou (CUT)

Date: 6/12/2021

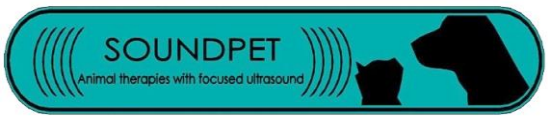

Ευρωπαϊκή Ένωση
Ευρωπαϊκά Διαρθρωτικά και Επενδυτικά Ταμεία

Κυπριακή Δημοκρατία

Διαρθρωτικά Ταμεία
της Ευρωπαϊκής Ένωσης στην Κύπρο

Contents

Executive summary

This deliverable describes the procedures implemented to assess the Magnetic Resonance (MR) compatibility of the transducer and robotic system. The report starts with a review of the work reported in the literature regarding the MR compatibility of various robotic devices. It then describes the methodology used in this work to evaluate the MR compatibility of ultrasonic motors, encoders, and transducers.

For MR compatibility assessment, four main sequences were used: the Fast Spin Echo (FSE), Fast Spoiled Gradient (FSPGR), SPGR and Echo Planar Imaging (EPI) sequences. The images were acquired under different activation states of the various components of the robot and transducer. To assess the MR compatibility, signal to noise ratio (SNR) measurements from a homogeneous phantom (GE coil phantoms) and an in-house agar-based phantom were used. A comprehensive analysis was also performed using guidelines from the American College of Radiology (ACR) and the corresponding phantom (ACR large phantom), which is used in MRI quality assurance programs worldwide. For image acquisition two set of coils were used; a General Purpose (GP) FLEX coil and a Body coil.

The developed robotic systems are classified as MRI-conditional according to American Society for Testing and Materials (ASTM) standards (F2503, F2052, F2213, F2182, and F2119) because the piezoelectric motors, optical encoders and transducers require electrical activation during operation.

Introduction

Magnetic resonance imaging (MRI) is the method of choice for accurately guiding High Intensity Focused Ultrasound (HIFU) procedures through MR thermometry. MR thermometry is a very challenging technique because it requires temperature changes calculation by post-processing MR images following HIFU. The challenges arise from the fact that specific hardware, including the piezoelectric actuators, motors, amplifiers, and other electronic circuits, may have to be operated before or during MR image acquisition. The latter is of particular importance in HIFU since real-time imaging is needed to monitor the temperature changes at the treatment location. It is therefore essential for robotic systems to be MR compatible, both in terms of MR safety but also in terms of acceptable effect on image quality, as well as to possess operational integrity that remains unaffected by the strong electromagnetic fields and gradients of the MR scanner [1].

One of the most obvious sources of interference are the ferromagnetic materials, which cause image artifacts and distortions and pose serious health hazards when placed in strong magnetic fields [2]. On the contrary, non-ferrous metals (e.g., titanium, brass, plastic, aluminum) are MR safe, but can also cause imaging artifacts [3]. Acrylonitrile Butadiene Styrene (ABS) and other three-dimensional printing materials are considered MR compatible [4].

HIFU robotic systems consist of a variety of hardware components that may interact with the MR field and cause imaging artifacts. Piezoelectric actuators can introduce artifacts to the MR image, despite that they are extensively used in MRI applications. The actuators are key components since they are responsible for robotic motion. For every motion type, an encoder is used to detect motion by signals' activation through the cables of the system. These can create artifacts by interrupting the local homogeneity of the MRI. Finally, the activation of the ultrasound (US) transducer during therapy can also cause artifacts [5,6].

According to the US Food and Drug Administration (FDA) and the ASTM, there are three levels of MRI device classification: MR safe, MR conditional and MR unsafe. The term 'MR safe' indicates equipment that does not pose any risk in the MR environment and does not introduce image artifacts. MR conditional items are considered safe under the specific conditions described by the product manufacturer, whereas the term 'MR unsafe' describes equipment that poses risk to the patient and/or the operator [7,8].

There are several factors to consider when engineering a robotic system for HIFU. Firstly, studies have shown that shielding the electronic parts of the robotic devices (e.g., motors, wiring) improves the SNR and avoids artifacts in MR images compared to systems without shielding [9, 10]. Furthermore, as mentioned above, activation of the encoders can also affect SNR. Studies have though shown a moderate effect of encoder's activation (even when it operates close to the magnet's isocenter) on the SNR, even when gradient echo (GRE) sequences are used [11, 12].

Another important factor is the choice of motor type. For example, the Shinsei motors cause a larger reduction in SNR compared to the Nanomotion motors, whereas the pneumatic actuators are ideal for MRI since they are non-magnetic (despite being very difficult to control) [2]. Nevertheless, studies have shown that even with the Shinsei motors, there are not significant reductions in SNR or visible image artifacts

[11]. Even the proximity of the piezoelectric motors to the isocenter must be considered. For example, if the motor is closer than 0.5 cm to the isocenter, it can generate image distortions. On the other hand, it has been demonstrated that distances bigger than 0.6 cm from the isocenter do not offer better SNR for specific motors, e.g., the Nanomotion motors. The reduction in SNR also depends on the choice of voltage levels and motor speed [13]. Moreover, the choice of magnet strength may also have a significant impact on image quality, with 1.5T scanners exhibiting larger SNR reductions compared to 3T scanners [2].

Lastly, the MR compatibility of the ultrasonic source should also be considered. Studies have shown that eddy currents may add noise to the image between the transducer and the sonicated tissue, whereas it seems that MRI interference from the HIFU beam does not occur in the sonication area [14]. Another study showed that ultrasonic probes with backing material disrupt the image only a few mm from the probe [15].

To assess the MR compatibility of robotic systems most studies employ sequences such as T1-weighted (T1W), T2-weighted (T2W), SE, FSE, GRE, FSPGR, and EPI [2, 9, 12].

Materials and Methods

Three robotic systems were tested for MR compatibility: the SOUNDPET robotic systems version 1 (v1), version 2 (v2), and version 3 (v3). The ultrasonic piezoelectric motors that drive the robotic devices are controlled by in-house electronic driving systems. Accordingly, the MR compatibility of the electronic systems (used to drive the robotic systems v1 and v2) was also evaluated. A single transducer (ID:24, Diameter: 38 mm, Radius of Curvature: 61 mm, frequency 2.6 MHz) was used in combination with the robotic systems v1 and v2, whereas a different US transducer (ID: 57, diameter: 50mm, radius of curvature: 65mm, frequency: 2.453 MHz) was incorporated in the robotic system v3.

The robotic systems were tested in a 1.5T MR system (Signa HDxt, General Electric, Fairfield, CT, USA). For the first assessment method (SNR measurements), image acquisition was performed with a general purpose (GP) FLEX coil (General Electric, Milwaukee, Wisconsin) and a body coil (12 Channel, GE Healthcare Coils, Aurora, Ohio, USA). For quality assurance using the ACR large phantom (J.M. Specialty Parts, San Diego, CA, USA), a split head coil (General Electric, Milwaukee, Wisconsin) was used instead. Three sequences were employed to assess the MRI compatibility: (1) T1W and T2W FSE sequences with fat suppression, (2) a FSPGR sequence and, (3) an EPI sequence. The experimental setup as well as the sequence parameters used in each case are presented in individual sections below.

MR compatibility assessment studies were carried out in a small homogeneous phantom provided by the vendor (GE small rectangular phantom) and an ACR large phantom.

Using the GE phantom, we have assessed the MR compatibility of the system by measuring the SNR of the phantom images at different activation states of the robotic system. The SNR was calculated using Equation 1

$$SNR = {SI_{phantom}}/{\sigma_{noise}} \quad [1]$$

where $SI_{phantom}$ is the mean signal intensity from a region of interest (ROI) within the imaged phantom and σ_{noise} is the standard deviation from a ROI placed in air (to measure the background noise of the image). For all the experiments, it was assumed that the noise in the MR images follows a Gaussian distribution.

A more comprehensive approach was followed for assessing MR compatibility according to the ACR MRI quality assurance program using the ACR large phantom. Individual tests were carried out to assess the geometric accuracy, high contrast spatial resolution, slice thickness accuracy, slice position accuracy, image intensity uniformity, percent signal ghosting, and low contrast object detectability.

Results

Image acquisition reproducibility

Before testing the MR compatibility of the equipment, we assessed the stability and reproducibility of the imaging sequences used. The small rectangular phantom was placed on the top of the MRI couch and covered with the GPFLEX coil. Five images were acquired for each of the following sequences: FSE, FSPGR, and EPI, under the same experimental conditions, and their SNR was calculated.

One-way ANOVA test was used to check for significant differences in the SNR between the acquired images for each sequence used. A non-parametric test (Kruskal-Wallis test) was used because there was no evidence that the data were normally distributed, following one-sample Kolmogorov-Smirnov test ($P \ll 0.01$).

Visual assessment of the acquired reference images did not show any significant change between them (images not shown in the report because they look identical). Figure 1 illustrates a bar chart of the measured SNR for each repeatability measurement for all three sequences. The results show that the FSE and EPI sequences offer a higher SNR compared to the FSPGR sequence.

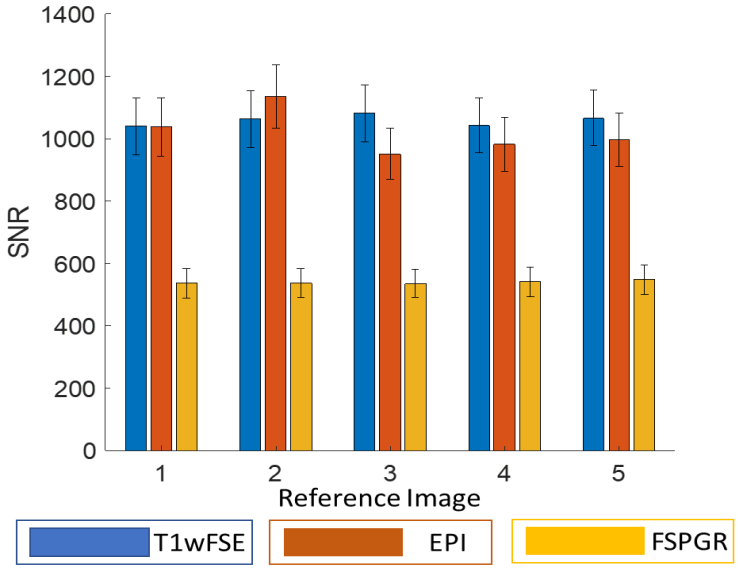

Figure 1. Bar Chart of measured SNR (with error bars) for five reference images acquired under the same experimental conditions for three different pulse sequences; FSE, EPI and FSPGR.

Despite that the SNR seems to be quite stable among reference images of the same sequence (by visual assessment), the one-way ANOVA test suggests that even without changing the experimental conditions (i.e., robot activation states) the SNR shows significant differences in some cases (shown in Figure 2, marked with ✗).

SNR test for FSE

Reference Image	1	2	3	4	5
1	-	✓	✗	✗	✗
2	✓	-	✗	✗	✗
3	✗	✗	-	✗	✗
4	✗	✗	✗	-	✗
5	✗	✗	✗	✗	-

SNR test for EPI

Reference Image	1	2	3	4	5
1	-	✗	✗	✗	✓
2	✗	-	✗	✗	✗
3	✗	✗	-	✓	✗
4	✗	✗	✓	-	✓
5	✓	✗	✗	✓	-

SNR test for FSPGR

Reference Image	1	2	3	4	5
1	-	✓	✓	✗	✗
2	✓	-	✓	✗	✗
3	✓	✓	-	✗	✗
4	✗	✗	✗	-	✗
5	✗	✗	✗	✗	-

Figure 2. One-way ANOVA that compares the SNR of each reference image with all the other reference images for significant difference. ✔ denotes there is no significance difference and ✗ suggests a significant difference at the 1% significance level.

The major reason for these differences is the random noise in the images, which causes the SNR to slightly change at every scan. The above statement was supported by further examining the signal intensity changes (instead of the SNR) among the several reference images. The same one-way ANOVA test shows that in most cases, the signal intensity is stable among MRI scans of the same sequence. The test results are presented in Figure 3.

Signal test for FSE

Reference Image	1	2	3	4	5
1	-	✓	✗	✓	✓
2	✓	-	✗	✓	✓
3	✗	✗	-	✗	✗
4	✓	✓	✗	-	✓
5	✓	✓	✗	✓	-

Signal test for EPI

Reference Image	1	2	3	4	5
1	-	✓	✓	✓	✓
2	✓	-	✓	✓	✓
3	✓	✓	-	✓	✓
4	✓	✓	✓	-	✓
5	✓	✓	✓	✓	-

Signal test for FSPGR

Reference Image	1	2	3	4	5
1	-	✗	✗	✗	✗
2	✗	-	✓	✓	✓
3	✗	✓	-	✓	✓
4	✗	✓	✓	-	✓
5	✗	✓	✓	✓	-

Figure 3. One-way ANOVA that compares the signal intensity of each reference image with all the other reference images for significant difference. ✔ denotes there is no significance difference and ✗ suggests a significant difference at the 1% significance level.

Overall, the results suggest that random variability of the SNR may occur among subsequent scans using one of the aforementioned sequences even under the same experimental conditions. Despite that, since the SNR changes are minimal (although significant) this methodology can be used for determining the SNR changes caused by varying experimental conditions (i.e., under different activation conditions of the robot) and not by random noise changes.

MR compatibility of the SOUNDPET Robotic System v1

To test the MR compatibility of the system upon activation of the transducer and amplifier, the small rectangular phantom from GE was used. Figure 4 shows the setup of the experiment. The SOUNDPET Robot v1 was placed on the MRI couch. The GE small rectangular phantom was placed at the acoustic opening and covered with the GPFLEX surface coil. The phantom was scanned using T1W and T2W FSE fat suppressed sequences (parameters listed in Table 1) under the following activation states:

I. Reference Image
II. Cables plugged, Amplifier OFF, Transducer OFF
III. Amplifier ON, Transducer OFF
IV. Amplifier ON, Transducer ON
V. Amplifier ON, Transducer ON, Power ON

Figure 4. (Left) SOUNDPET Robot v1 (i) positioned on the MRI table. A homogeneous MR phantom (ii) was positioned on the device and covered by the GPFLEX surface coil (iii). (Right) Cables connected on the MRI panel (arrows); cable in black was connected to the motor and cable in grey was connected to the encoder.

Figure 5 and Figure 6 illustrate the T1W and T2W images acquired under the activation states specified above. The SNR of the T1W and T2W images under condition V (Amplifier ON, Transducer ON, and Power ON) decreased by approximately 90% and 80%, respectively, compared to the reference image (i.e., state I). The SNR differences between states I, II and III are smaller.

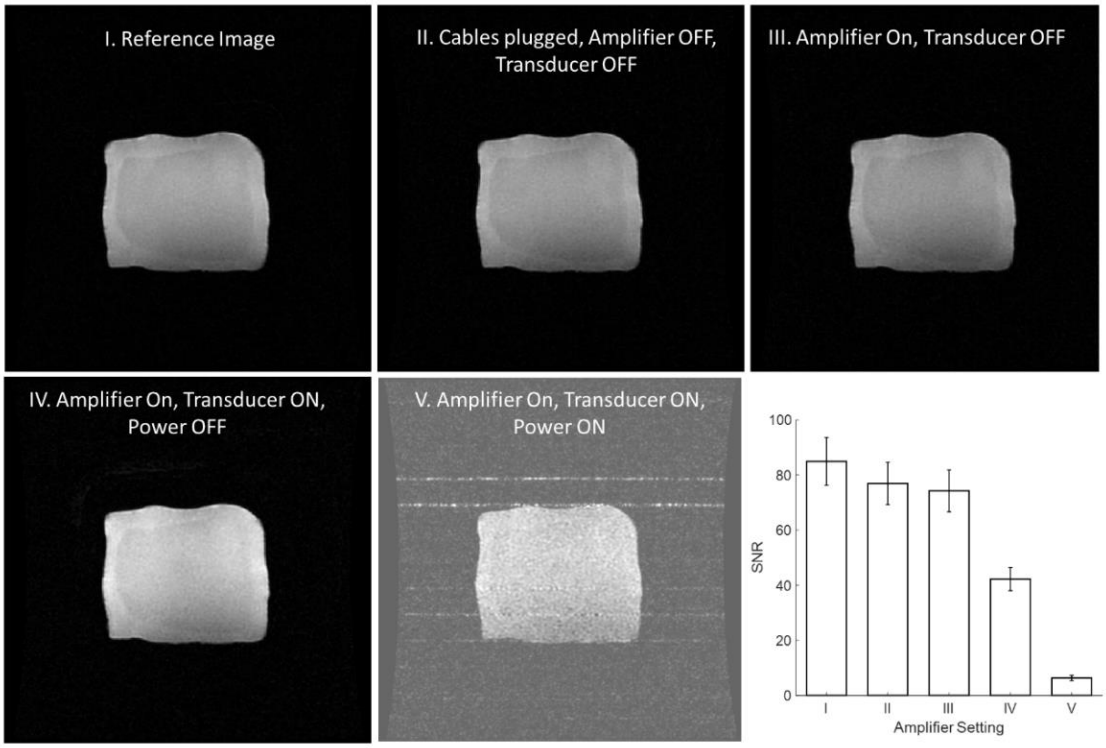

Figure 5. Axial slice acquired using a 2D T1W FSE sequence (TE: 9.2 ms, TR: 200 ms, in plane resolution: 0.5x0.5 mm, slice thickness: 4 mm, pixel bandwidth: 75.1 Hz, ETL: 3, NEX: 1) under difference activation settings of the Robotic System v1. At the right corner, a bar chart of SNR (with error bars) for the different activation states is shown.

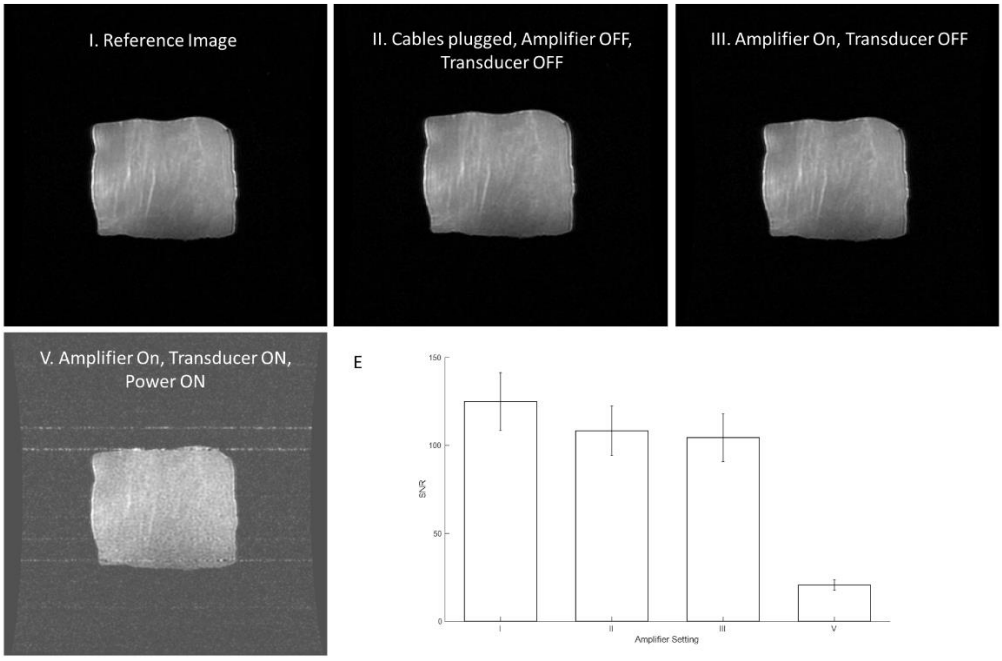

Figure 6. Axial slice acquired using a 2D T2W FSE sequence (TE: 87.9 ms, TR: 2000 ms, in plane resolution: 0.5x0.5 mm, slice thickness: 4 mm, pixel bandwidth: 81.4 Hz, ETL: 12, NEX: 4) under different activation settings of the Robotic System v1. At the right corner, a bar chart of SNR (with error bars) for the different activation states is shown.

Table 1: Sequence and Parameters for MR Imaging.

Sequences	Coil	Acquisition Type	TR (ms)	TE (ms)	Flip Angle (degrees)	Echo Train Length	Pixel Bandwidth	Field of View (mm^3)	Slice Spacing (mm)	Reconstruction Matrix Size	No. of Averages	Acquisition Time (s)
T2W FSE FS	Flex Surface Coil	2D	2000	88	90	12	81.4	260x260x4	0.1	224x192	4	45
T1W FSE FS	Flex Surface Coil	2D	200	9.2	90	2	75.1	260x260x4	0.1	224x192	3	45

Visual assessment reveals that when Power was ON, RF interference occurred. This appears as a series of zipper artifacts in multiple rows of the image. At the same time, the image signal is compromised compared to the other activation conditions.

MR compatibility of the SOUNDPET Robotic System v1 using two different Electronic Systems

The experimental setup used in this experiment was the same as the one shown in Figure 4. The methodology was similar, with the only difference that the phantom was scanned using FSE, FSPGR, and EPI sequences (parameters listed in Table 2) under the following activation states:

I. Reference Image
II. Cables plugged in the SOUNDPET Robot v1.
III. Electronic system 1 motor driver switched ON.
IV. Electronic system 1 motor energized.
V. Electronic system 2 (Arduino) motor driver switched ON.
VI. Electronic system 2 (Arduino) motor energized.

Table 2: Sequence and Parameters for MR imaging.

Sequences	Type	Coil	Acquisition Type	TR (ms)	TE (ms)	Flip Angle (degrees)	Echo Train Length	Pixel Bandwidth	Field of View (mm^3)	Slice Spacing (mm)	Reconstruction Matrix Size	No. of Averages	Acquisition Time/Slice (s)
FSPGR	Gradient Echo	Flex Surface	2D	40	13	30	1	244.1	260x260x5	0.1	192x192	1	7.3
EPI	Gradient Echo	Flex Surface	2D	80	19	25	1	7812.5	260x260x5	0	64x64	2	0.2
FSE FS	Spin Echo	Flex Surface	2D	200	9.2	90	2	75.1	260x260x4	0.1	224x192	2	11

The electronic system 1 (Figure 7A) controls four small motors, whereas the electronic system 2 (Figure 7B) controls one small motor. The SNR was estimated for each set of images (i.e., set of images acquired for each tested sequence) as explained in the Materials and Methods section using equation (1).

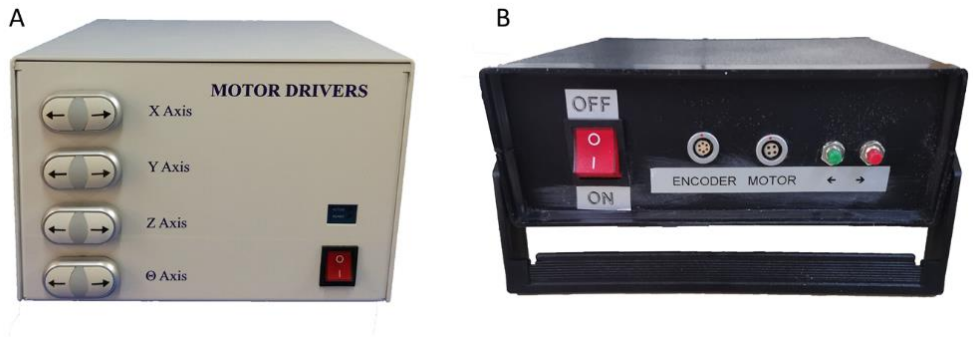

Figure 7. (A) Electronic system 1, (B) Electronic system 2.

The phantom images acquired using the FSE, EPI, and FSPGR sequences under different activation conditions of the robotic system v1 are shown in Figure 8 to Figure 10, respectively. Visual assessment of the acquired images does not show any significant effect on image quality between the various activation conditions. Figure 11 illustrates the effect of the various activation settings on the measured SNR for each tested sequence, for both electronic systems used.

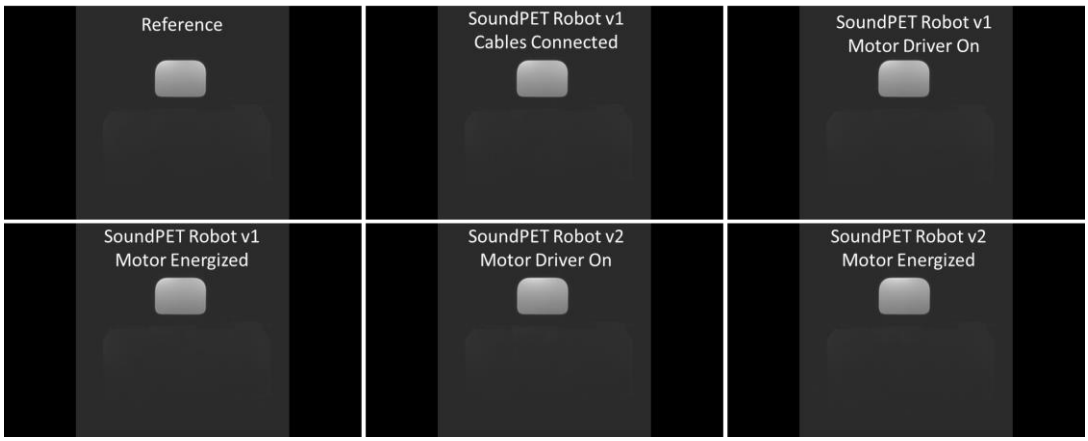

Figure 8. Axial image acquisition using FSE sequence for different activation conditions.

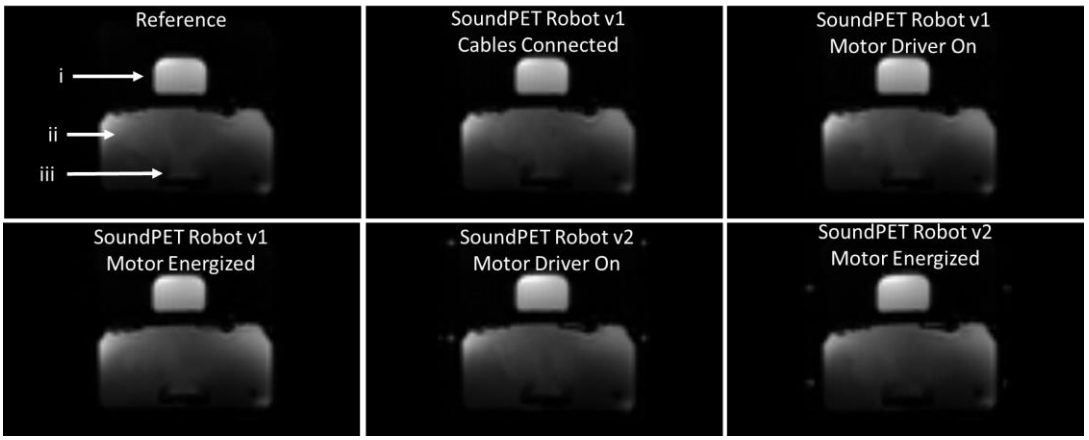

Figure 9. Axial image acquisition using EPI sequence for different activation conditions. (i) Small rectangular phantom, (ii) Water container of the SOUNDPET Robot v1, and (iii) US transducer.

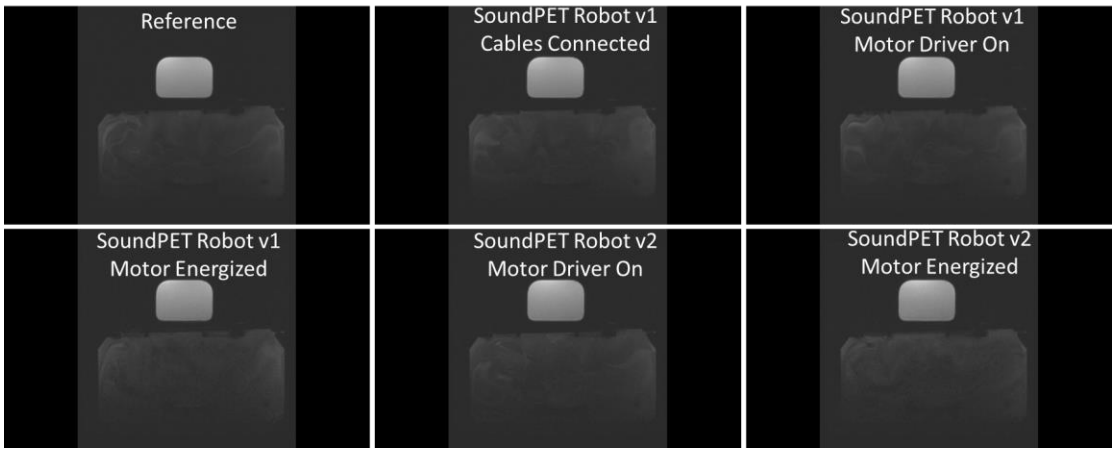

Figure 10. Axial image acquisition using FSPGR sequence for different activation conditions.

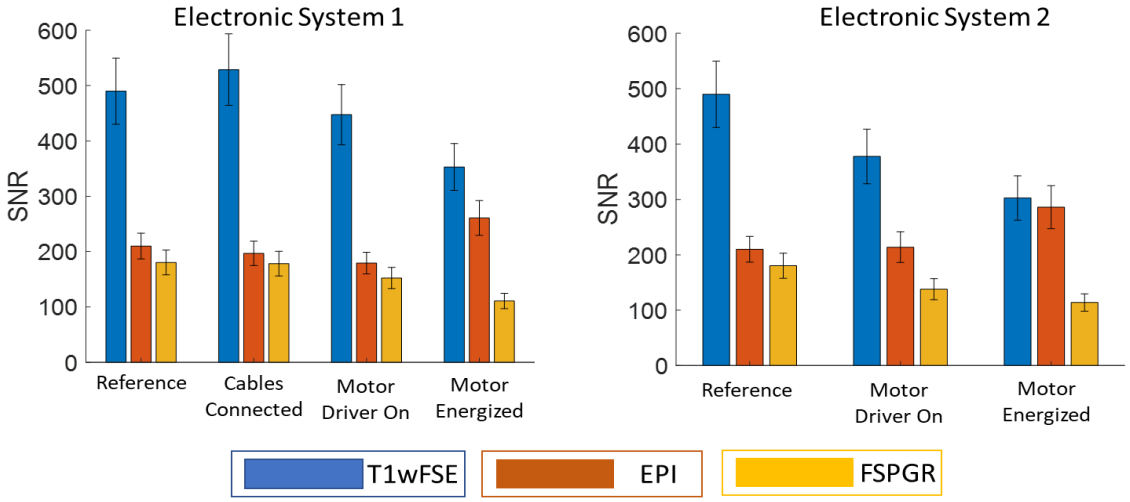

Figure 11. Bar Chart of measured SNR (with error bars) for the various robot activation states for both electronic systems used and different pulse sequences; FSE, EPI and FSPGR.

MR compatibility of the SOUNDPET Robotic System v2

The MR compatibility of the robotic system v2 was then assessed using similar methodology. The experimental setup used in this experiment was the same as the one shown in Figure 4, but a different electronic system designed to control large motors (Figure 12) was instead used. Again, the phantom was scanned using FSE, FSPGR, and EPI sequences (parameters shown in Table 2) under the following activation states:

I. Reference Image.
II. Cables plugged in the SOUNDPET Robot v2.
III. Electronic system motor driver switched ON.
IV. Interface connected.
V. Motor energized.

Figure 12. Electronic system for large motors.

The phantom images acquired using the FSE, EPI, and FSPGR sequences under different activation conditions of the robotic system v2 are shown in Figure 13 to Figure 15, respectively. Visual assessment of the acquired images does not show any significant effect on image quality between the various activation conditions. Figure 16 illustrates the effect of the various activation states on the measured SNR for all tested sequences.

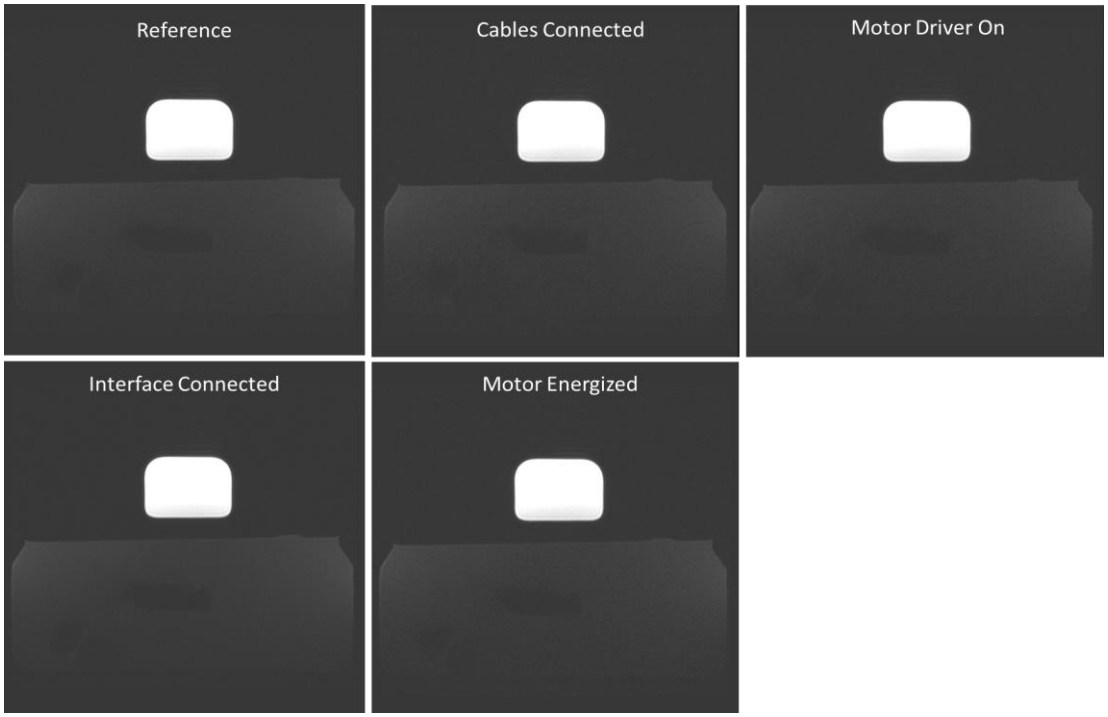

Figure 13. Axial image acquisition using FSE sequence for different activation conditions.

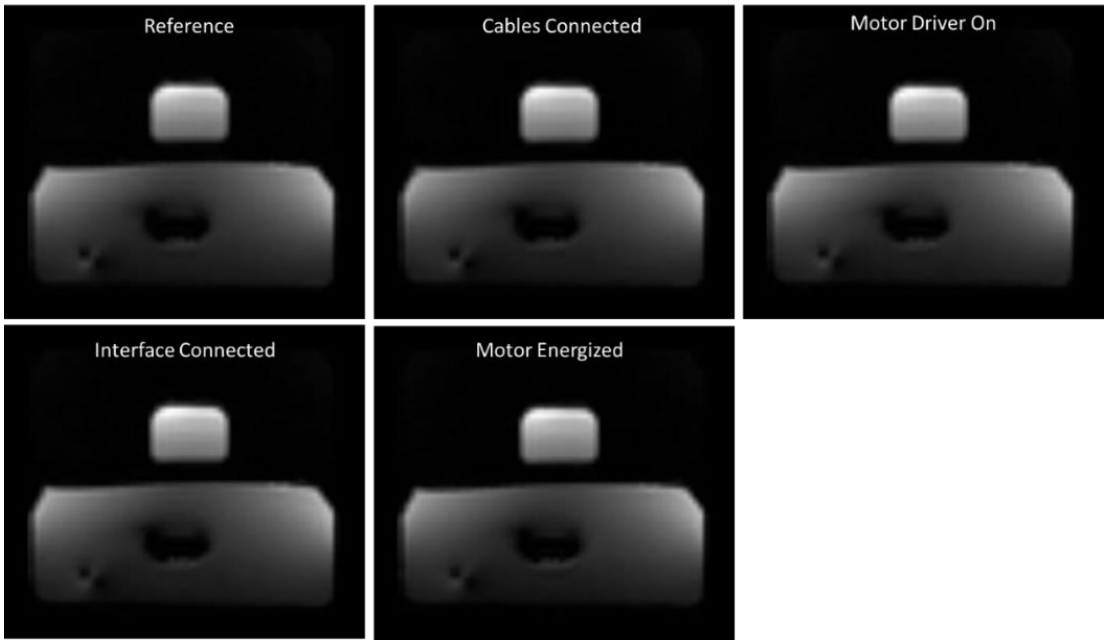

Figure 14. Axial image acquisition using EPI sequence for different activation conditions.

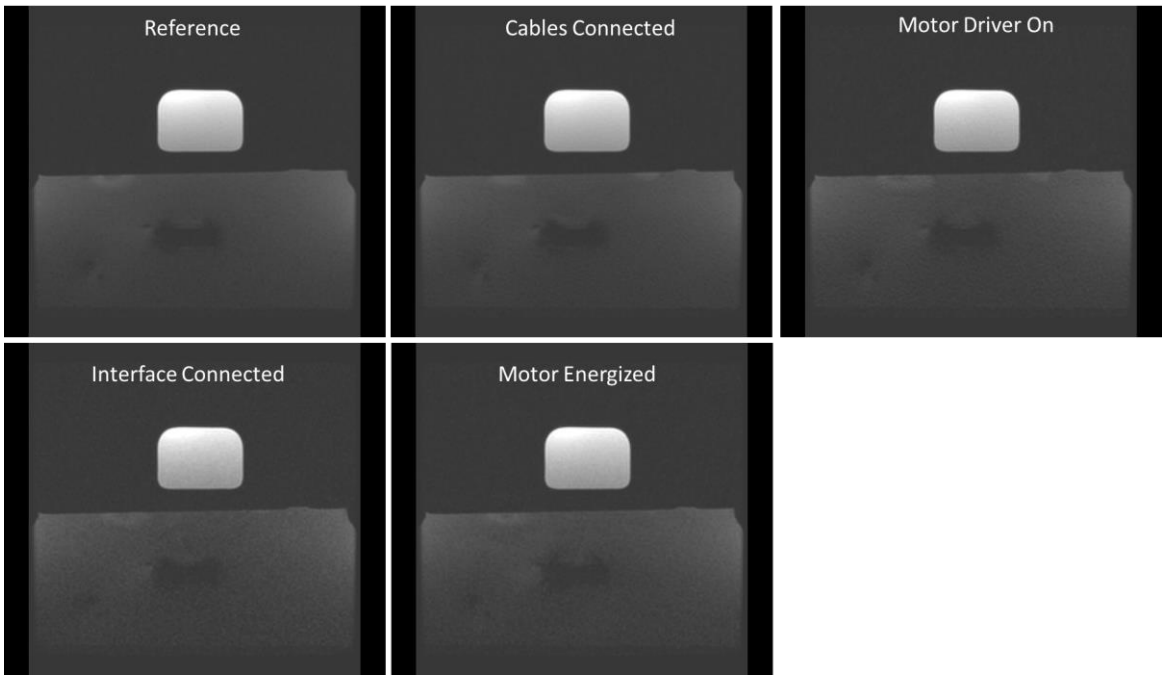

Figure 15. Axial image acquisition with FSPGR sequence for different activation conditions.

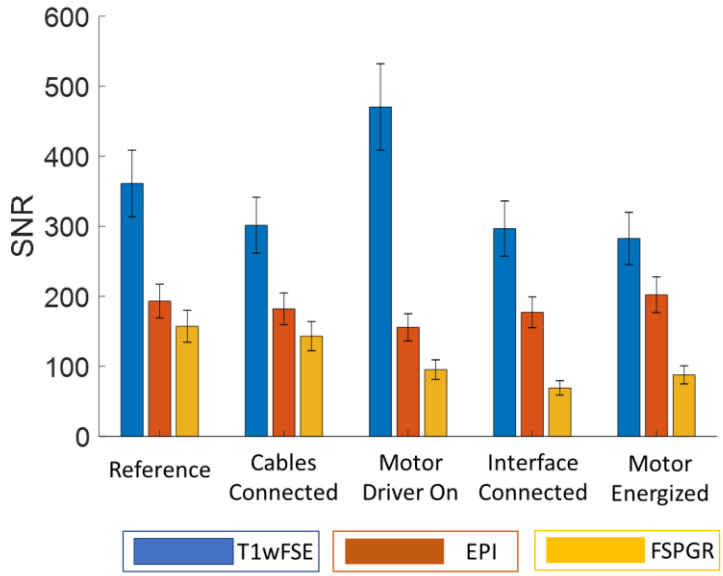

Figure 16. Bar Chart of measured SNR (with error bars) for the various robot activation states for different pulse sequences; FSE, EPI and FSPGR (Robotic system v2).

MR compatibility of the SOUNDPET Robotic System v2: Coil position effect

The aim of this test was to assess the image quality for two different coil positions; (1) in close proximity to the top surface of the meat (as in most of the experiments reported herein) and (2) at a distance from the upper surface of the raw meat. The latter condition is shown in Figure 17. For MR image acquisition, a fat suppressed FSE sequence was used with the following parameters: TR: 400 ms, TE: 13 ms, FA: 90^0, ETL: 3, BW: 27.11, FOV: 320×320×8, matrix: 128×128, and acquisition time per slice: 34.6 s.

Figure 17. SOUNDPET Robot v2 (i) positioned on the MRI table. A piece of raw meat was placed at the acoustic opening above the US transducer. A rectangular positioner (ii) was used to increase the distance between the transducer and the coil (iii).

The scans were initially performed with the coil positioned in close proximity to the top surface of the meat. Different powers in the range of 2 to 150 W were applied to assess the effect on image quality. Then, imaging was repeated with the coil placed at a distance from the meat. The following activation states were tested:

I. Reference Image - No cables connected to the transducer
II. Cables connected to the transducer
III. Amplifier On
IV. Power set to 2 W
V. Power set to 5 W
VI. Power set to 10 W
VII. Power set to 15 W
VIII. Power set to 20 W
IX. Power set to 50 W
X. Power set to 100 W
XI. Power set to 150 W

Figure 18 shows an example of images acquired with the flex surface coil positioned in close proximity to the top of the meat. Visual assessment of the acquired images reveals a severe reduction in image quality with increasing applied power, with difficulty in locating the focal heating spot.

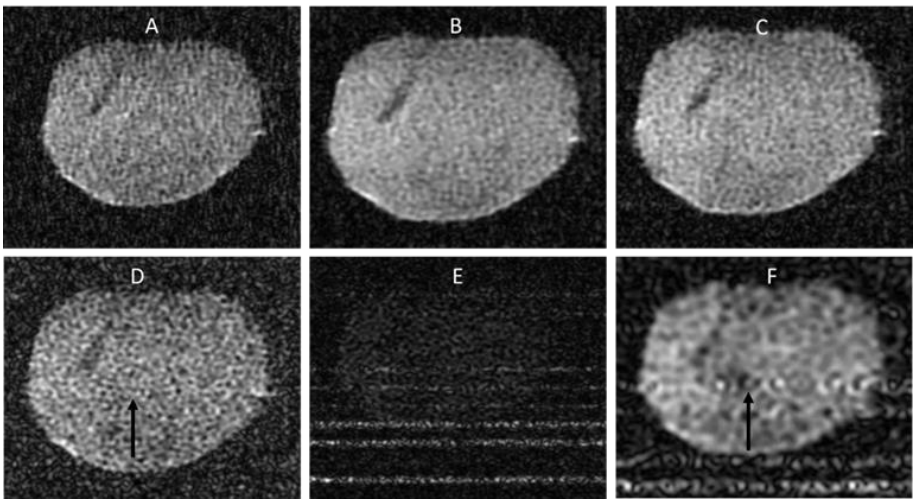

Figure 18. T1W FSE axial images acquired with the general-purpose flex surface coil close to the top of the meat. (A) Power of 2 W for 30s (TR=200ms), (B) Power of 5W (TR=300ms), (C) Power of 10W (TR=300ms), (D) Power of 20W (TR=300ms), (E) Power of 50W (TR=300ms), (F) Power of 50W (TR=400ms). Arrow indicates focal spot.

Figure 19 shows the images acquired with the coil positioned at a distance from the meat and the transducer. The image quality is visibly improved compared to when the coil is in close proximity to the meat.

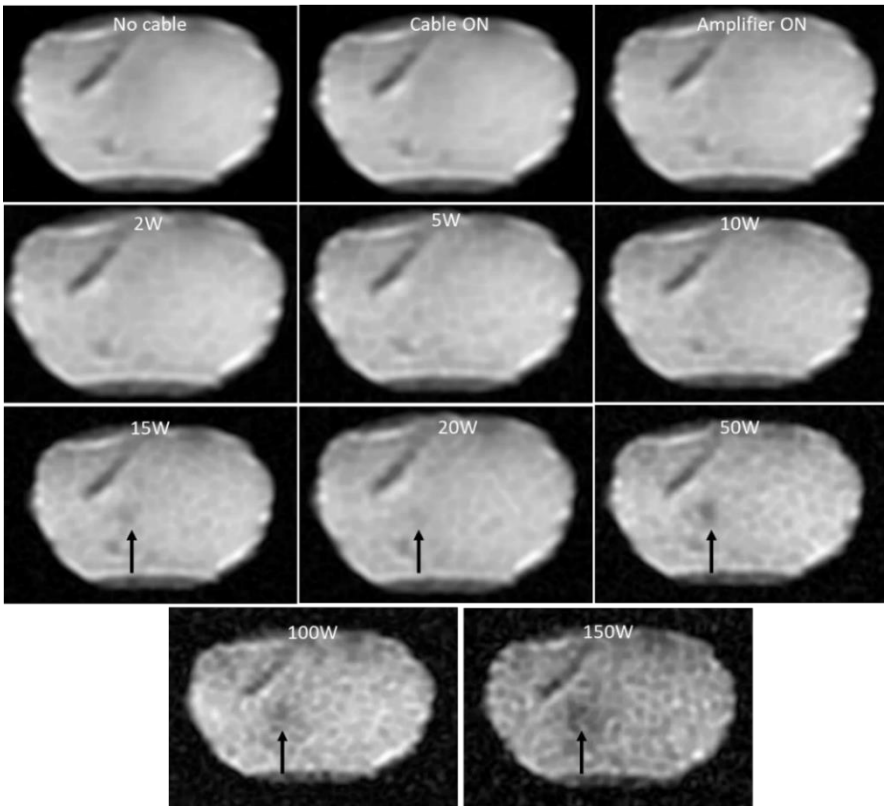

Figure 19. T1W FSE axial images for various activation states, with the coil at a distance from the meat. Arrow indicates focal spot.

Figure 20 and Figure 21 show the corresponding SNR and signal intensity measurements, respectively, for the different activation states shown in Figure 19. As expected, the SNR reduces as the power of the transducer is increased.

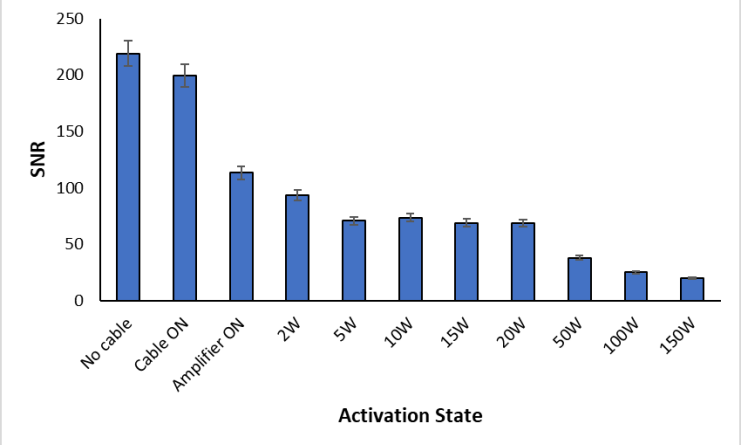

Figure 20. Bar chart of SNR (with error bars) for different activation states.

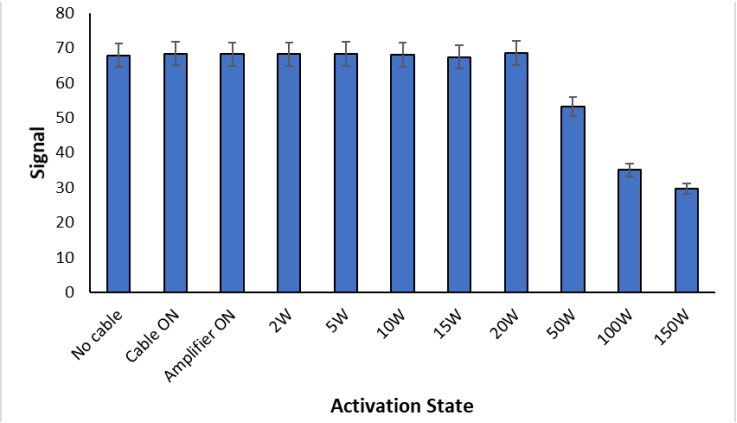

Figure 21. Bar chart of signal intensity (with error bars) for different activation states.

MR compatibility of the SOUNDPET Robotic System v2 using the ACR large phantom

The purpose of the experiment was to assess the MR compatibility of the SOUNDPET Robot v2 using the ACR guidelines for MRI quality assurance. The ACR MRI large phantom was imaged. Figure 22 shows the setup of the experiment. The SOUNDPET Robot v2 was placed on the MRI couch and the ACR phantom was positioned near the front of the device, in proximity to the transducer. The phantom was scanned with the split head coil using a T1W SE sequence in the axial plane under the following robot activation states:

I. Reference Image.
II. No Cables plugged in the SOUNDPET Robot v2.
III. Cables plugged in the SOUNDPET Robot v2.
IV. Interface connected and motor driver switched ON.
V. Motor Energized.

The analysis was performed according to the guidelines published by the ACR, as described in the Phantom Test Guidance document for the ACR MRI Accreditation Program. The individual tests carried out for accuracy assessment are next presented.

Figure 22. SOUNDPET Robotic System v2 positioned on MRI table. The ACR phantom was placed inside the split head coil close to the robot.

Geometric Accuracy

The geometric accuracy test assesses the accuracy with which the image represents distances in the imaged subject. Distance measurements of the phantom diameter were made in 4 directions (top to bottom, left to right, and both diagonals), as shown in Figure 23, and then, the results were compared with the known distance values. Notably, for the sagittal localizer, only a reference image was acquired. Table 3 lists the geometric accuracy measurements and their difference from the expected values. All measured distances should be within ± 2mm of their true values.

Table 3. Geometric accuracy measurements having as a criterion a difference ≤ 2mm.

Activation State	Geometric Accuracy Measurement													
	Sagittal Localizer		A/P [Sl. #1]		R/L [Sl. #1]		A/P [Sl. #5]		R/L [Sl. #5]		Diag. 1 [Sl. #5]		Diag. 2 [Sl. #5]	
-	Measured	Diff.	Measured	Diff.	Measured	Diff.	Measured	Diff.	Measured	Diff.	Measured	Diff.	Measured	Diff.
Reference Image	148	0	191	1	190	0	191	1	190	0	190	0	190	0
No Cables	-	-	191	1	190	0	191	1	190	0	190	0	190	0
Cables ON	-	-	191	1	190	0	191	1	190	0	190	0	190	0
Interface Connected&Motor Driver ON	-	-	191	1	190	0	191	1	190	0	190	0	190	0
Motor Energized	-	-	191	1	190	0	191	1	190	0	190	0	190	0

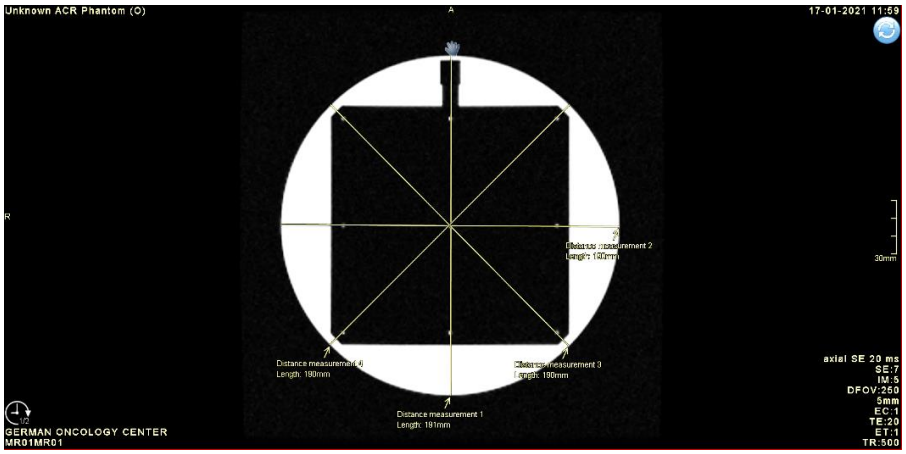

Figure 23. Slice 5 with diameter measurements illustrated.

High Contrast Spatial Resolution

The test assesses the scanner's ability to resolve small objects when the contrast to noise ratio is sufficiently high. For this test, the distinguishability of closely spaced small bright spots arranged in arrays is visually assessed. Figure 24 shows the resolution insert (a small plastic block) with 3 pairs of hole arrays. Each pair of hole arrays consists of an upper left (UL) hole array and a lower right (LR) hole array. There is no quantitative analysis for this assessment, but what is required is that all 4 holes in at least 1 row/column are distinguishable/ recognizable as points of brighter signal intensity compared to the spaces between them. Table 4 lists the results of the visual assessment.

Table 4. High Contrast Spatial Resolution measurements having as a criterion the visual assessment of holes.

Activation State	Resolution (mm)	High Contrast Spatial Resolution								
		R-L (UL)				A-P (LR)				Overall
		1	2	3	4	1	2	3	4	
Reference Image	1.1	✓	✓	✓	✓	×	×	✓	✓	✓
	1	✓	✓	✓	✓	×	×	×	✓	✓
	0.9	×	×	×	×	×	×	×	×	×
No Cables	1.1	✓	✓	✓	✓	✓	✓	✓	×	✓
	1	✓	✓	✓	✓	×	×	×	✓	✓
	0.9	×	×	×	×	×	×	×	×	×
Cables On	1.1	✓	✓	✓	✓	×	×	✓	✓	✓
	1	✓	✓	✓	✓	×	×	×	×	✓
	0.9	×	×	×	×	×	×	✓	×	✓
Interface Connected&Motor Driver On	1.1	✓	✓	✓	✓	×	×	✓	✓	✓
	1	✓	✓	✓	✓	×	×	×	✓	✓
	0.9	×	×	×	×	×	×	×	×	×
Motor Energized	1.1	✓	✓	✓	✓	✓	✓	✓	✓	✓
	1	×	✓	✓	✓	×	×	×	✓	✓
	0.9	×	×	×	×	×	×	×	×	×

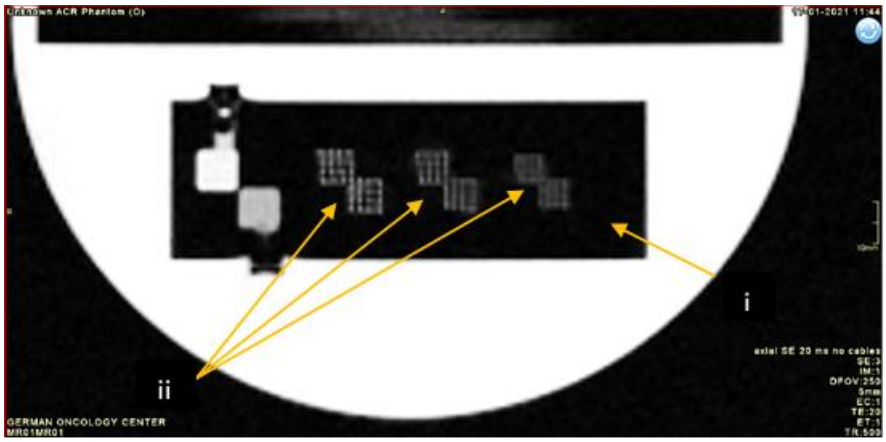

Figure 24. Slice 1 showing the resolution insert (i) and three pairs of hole arrays (ii).

Slice Thickness Accuracy

The slice thickness accuracy test assesses the accuracy with which a slice of specified thickness is achieved. The prescribed slice thickness is compared with the measured slice thickness. Figure 25 shows the signal ramps of the slice thickness insert with the ROIs used for measuring the average signal in the ramps, and their length measurements. The slice thickness was calculated using Equation 2:

$$slice\ thickness = 0.2\ x\ (top\ x\ bottom)/(top + bottom) \quad [2]$$

All measured slice thicknesses should be 5.0 mm ± 0.7 mm (Table 5).

Table 5. Slice thickness accuracy measurements having as a criterion slice thickness within 5.0 ± 0.7 mm.

Activation States	Slice Thickness Accuracy								
	Mean Ramp Signal			Preprocessing Contrast Adjustments		Ramp Length Measurements (mm)		Slice Thickness (mm)	
-	Top	Bottom	Overall	Window	Level	Top	Bottom	Measurement	Diff. (≤0.7 mm)
Reference Image	186	189	187.5	1	93.75	47.8	47	4.74	0.26
No Cables	184	201	192.5	1	96.25	45	46	4.55	0.45
Cables On	186	184	185	1	92.5	44.4	46.1	4.52	0.48
Interface Connected&Motor Driver On	189	201	195	1	97.5	43.5	46.2	4.48	0.52
Motor Energized	190	198	194	1	97	43.3	45	4.41	0.59

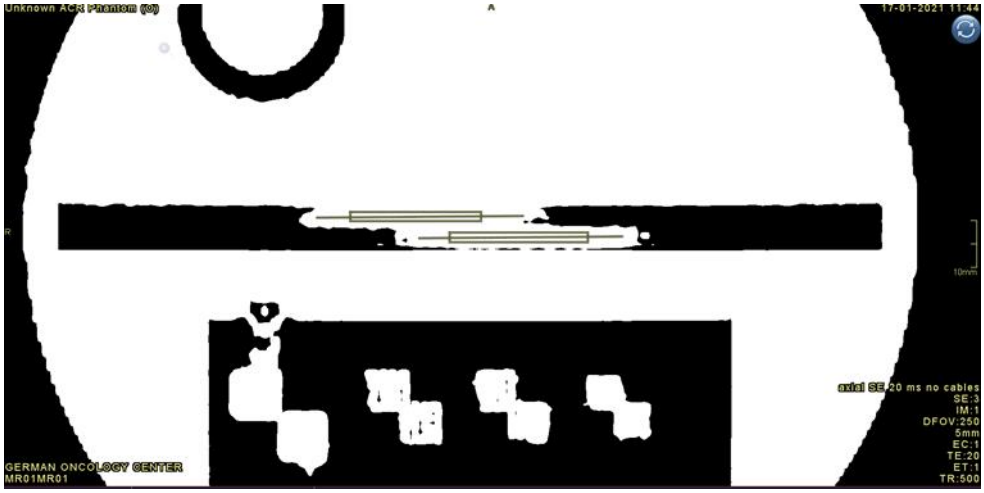

Figure 25. Magnified region of slice 1 showing slice thickness signal ramps with ROIs placed for measuring average signal in the ramps.

Slice Position Accuracy

This test assesses the accuracy with which slices can be prescribed at specific locations utilizing the localizer image for positional reference. For this test, the differences between the prescribed and actual positions of slices 1 and 11 are measured. Figure 26 shows the images of slices 1 and 11 illustrating measurement of slice position error. If the bar on the right is longer meaning the slice is mispositioned superiorly, this bar length difference is assigned a positive value, otherwise (i.e., if the bar on the left is longer), meaning the slice is mispositioned inferiorly, is assigned a negative value.

Table 6 lists the slice position accuracy measurements. All measurements of the absolute bar length differences should be 5 mm or less.

Table 6. Slice position accuracy measurements having as a criterion bar length differences ≤ | 5 mm | (advisable ≤ | 4 mm |).

Activation States	Slice Position Accuracy				
	Measured Difference (mm)		Actual Difference (mm)		
-	Slice 1	Slice 11	Slice 1	Slice 11	Direction
Reference Image	-1.2	0	-0.6	0	*Inferior*
No Cables	-1.1	-0.4	-0.55	-0.2	*Inferior*
Cables On	-1.5	0	-0.75	0	*Inferior*
Interface Connected&Motor Driver On	-1.6	0	-0.8	0	*Inferior*
Motor Energized	-1.5	-0.2	-0.75	-0.1	*Inferior*

Figure 26. (Top) Slice 1 and (Bottom) Slice 11 illustrating measurements of slice position errors.

Image Intensity Uniformity

The image intensity uniformity test measures the uniformity of the image intensity over a large water area of the phantom near the middle of the imaged volume, thus near the middle of the head coil. For this test, the high and low signal levels within a large ROI in a water area of the phantom are measured. Figure 27 shows how the lowest and highest signal ROIs are positioned in the image. Equation 3 was used to estimate the percent integral uniformity (PIU):

$$PIU = 100x(1 - \left\{\frac{high-low}{high+low}\right\}) \quad [3]$$

Table 7 lists that image intensity uniformity measurements. All measured values of PIU should be ≥ 87.5%.

Table 7. Image intensity uniformity measurements having as a criterion a PIU ≥ 87.5%.

Activation States	Slice No.	Image Intensity Uniformity						
		Large ROI		Low Intensity ROI		High Intensity ROI		Percent Intensity Uniformity
-	-	Area (cm^2)	Mean	Area (cm^2)	Mean	Area (cm^2)	Mean	PIU
Reference Image	# 7	200	1012	1	956	1	1044	95.60%
No Cables	# 7	200	1025	1	975	1	1052	96.20%
Cables On	# 7	200	1027	1	974	1	1054	96.06%
Interface Connected&Motor Driver On	# 7	200	1029	1	975	1	1054	96.11%
Motor Energized	# 7	200	1029	1	975	1	1058	95.92%

Figure 27. Image of slice 7 showing the large (200 cm²) and the small (1 cm²) ROIs. (Top) Example of measuring the mean signal of low intensity. (Bottom) Example of measuring the mean signal of high intensity.

Percent Signal Ghosting

The percent-signal ghosting test assesses the level of ghosting in the images. Ghosting is an artifact in which a faint copy (the ghost) of the imaged object appears superimposed on the image, displaced from its true location. Ghosting is a consequence of signal instability between pulse cycle repetitions. Figure 28 shows the main ROI that is placed and the four elliptical ROIs along the 4 edges of the field of view. The value of the ghosting ratio was calculated using Equation 4:

$$ghosting\ ratio = |((top + btm) - (left + right))/(2\ x\ large\ ROI)| \quad [4]$$

Table 8 lists the percent signal ghosting measurements. The percent signal ghosting ratio (PSG) for all states should be ≤ 2.5%.

Table 8. Percent Signal Ghosting measurements having as a criterion a PSG ≤ 2.5%.

Activation States	Slice No.	Percent Signal Ghosting										
		Centre ROI		Top ROI		Bottom ROI		Right ROI		Left ROI		Percent Signal Ghosting
-	-	Area (cm^2)	Mean	ea (cr	Mean	Area (cm^2)	Mean	Area (cm^2)	Mean	Area (cm^2)	Mean	PSG
Reference Image	# 7	200	1012	10	24.8	10	26	10	26.6	10	25.8	0.08%
No Cables	# 7	200	1025	10	25	10	26.6	10	25.9	10	26	0.01%
Cables On	# 7	200	1027	10	26.7	10	26.6	10	26.7	10	25.4	0.06%
Interface Connected&Motor Driver On	# 7	200	1029	10	26.4	10	26.7	10	27.7	10	26	0.03%
Motor Energized	# 7	200	1029	10	26.6	10	26.7	10	26.4	10	26.7	0.01%

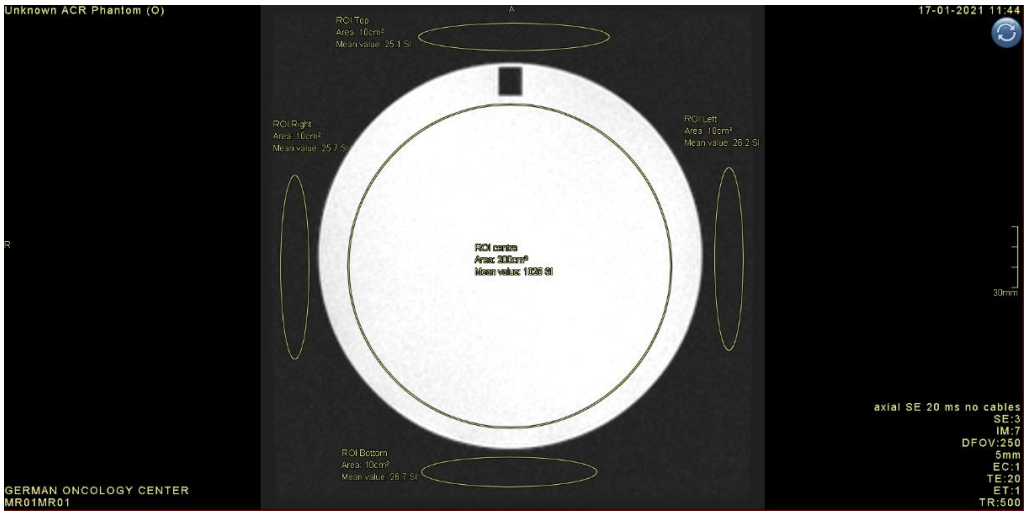

Figure 28. Image of slice 7 illustrating ROIs placement for percent signal ghosting measurements.

Low Contrast Object Detectability

The low contrast object detectability test assesses the extent to which objects of low contrast are distinguishable in the images. For this purpose, the phantom has a set of low contrast objects of varying size and contrast. These low contrast objects appear on 4 slices (8 through 11) of the phantom each one having 10 spokes of disks, and each spoke is made up of 3 disks. From slice 8 to slice 11 the contrast values for each disk are 1.4%, 2.5% , 3.6% and 5.1%, respectively. For this test we counted the number of spokes that were completely visible. A spoke is complete only if all 3 disks are discernible. Figure 29 shows low contrast objects of slice 11. For each activation state, the number of complete spokes in each slice was scored. Table 9 lists the low contrast object detectability measurements. At least 9 spokes should be visible.

Table 9. Low Contrast Object Detectability measurements having as a criterion the visual assessment of the spokes. The target score for the images is at least 9 visible spokes.

Activation States	Slice No.	Contrast Value	Low Contrast Object Detectability SPOKE # 1	2	3	4	5	6	7	8	9	10	Total Spokes Resolve
Reference Image	#11	5.1%	✓	✓	✓	✓	✓	✓	×	×	✓	×	17
	#10	3.6%	✓	✓	✓	✓	✓	✓	×	×	×	×	
	#9	2.5%	✓	✓	✓	✓	×	×	×	×	×	×	
	#8	1.4%	×	×	×	×	×	×	×	×	×	×	
No Cables	#11	5.1%	✓	✓	✓	✓	✓	✓	✓	✓	×	×	20
	#10	3.6%	✓	✓	✓	✓	✓	✓	✓	×	×	×	
	#9	2.5%	✓	✓	✓	✓	✓	×	×	×	×	×	
	#8	1.4%	×	×	×	×	×	×	×	×	×	×	
Cables On	#11	5.1%	✓	✓	✓	✓	✓	✓	✓	✓	×	×	22
	#10	3.6%	✓	✓	✓	✓	✓	✓	✓	✓	✓	×	
	#9	2.5%	✓	✓	✓	✓	×	✓	×	×	×	×	
	#8	1.4%	×	×	×	×	×	×	×	×	×	×	
Interface Connected &Motor Driver On	#11	5.1%	✓	✓	✓	✓	✓	✓	✓	✓	✓	×	23
	#10	3.6%	✓	✓	✓	✓	✓	✓	✓	✓	×	×	
	#9	2.5%	✓	✓	✓	✓	✓	×	×	×	×	×	
	#8	1.4%	✓	×	×	×	×	×	×	×	×	×	
Motor Energized	#11	5.1%	✓	✓	✓	✓	✓	✓	✓	✓	×	×	18
	#10	3.6%	✓	✓	✓	✓	✓	✓	✓	×	✓	×	
	#9	2.5%	✓	✓	×	×	×	×	×	×	×	×	
	#8	1.4%	×	×	×	×	×	×	×	×	×	×	

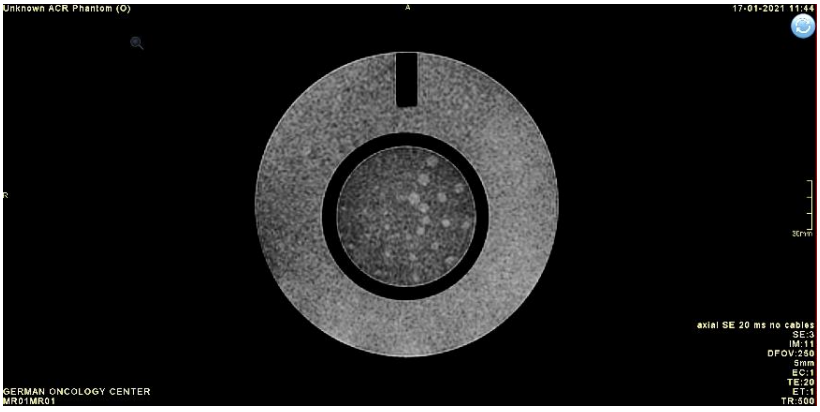

Figure 29. Image of slice 11 showing the low-contrast objects for the low contrast object detectability test.

MR compatibility of the SOUNDPET Robotic System v2 using two different coils

The purpose of this evaluation was to assess the MR compatibility of the SOUNDPET Robot v2 using two different coils, the GP FLEX coil, and the body coil. The robot was placed on the MRI table and an agar-based phantom (6 % w/v agar) was placed in the acoustic opening of the water container above the US transducer (ID: 24, diameter: 38mm, radius of curvature: 61mm, frequency: 2.6 MHz), as shown in Figure 30. The US transducer was connected to the amplifier AG1016 (AG Series Amplifier, T & C Power Conversion, Inc., Rochester, US). Several MR compatible objects were used to increase the distance between the coil and the phantom (Figure 30).

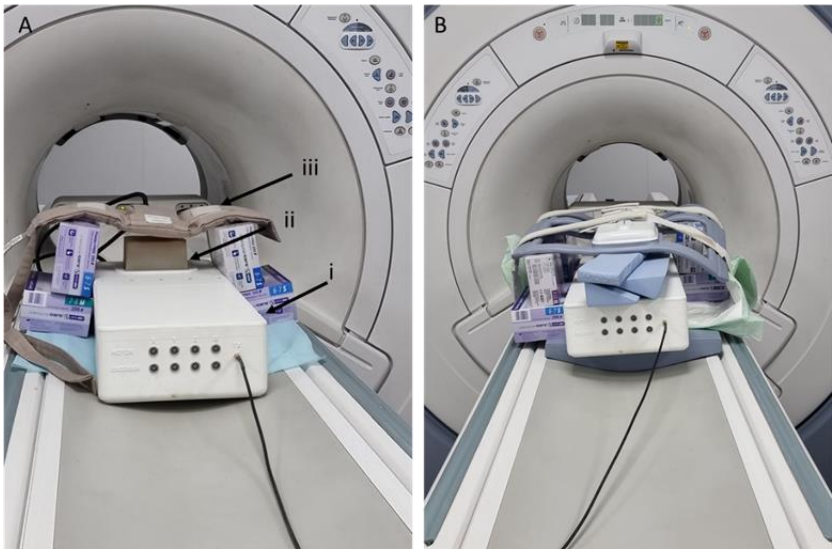

Figure 30. SOUNDPET Robot v2 (i) positioned on the MRI table. (A) An agar-based phantom (ii) was placed in the acoustic opening above the US transducer and covered with the multi-purpose flex surface coil (iii). (B) Phantom covered with the body coil.

For MR image acquisition, SPGR and FSE sequences were used (parameters listed in Table 10). To assess the effect of different coils and sequences, the following activation states were implemented:

I. Reference Image – No amplifier cable connected to the robot
II. Amplifier cable connected to the robot
III. Amplifier ON
IV. Power set to 100 W
V. Power set to 200 W

Table 10. Sequence and Parameters for MR Imaging

Sequences	Type	Coil	Acquisition Type	TR (ms)	TE (ms)	TI (ms)	Flip Angle (degrees)	Echo Train Length	Pixel Bandwidth(Hertz /pixel)	Field of View (mm^3)	Acquisition Matrix Size(freq× phase)	No. of Averages	Acquisition Time/Slice (s)
SPGR	GE	Body & Flex Surface	2D	29	12.5	-	30	1	31.01	280x280x10	160x160	1	4.8
T1 FSE FS	Spin Echo	Body&Flex Surface	2D	200	13.21	-	90	5	39.06	280x280x6	192x128	2	12.6

A ROI approach was used to measure the SNR as explained in the Material and Methods section. Figure 31 shows an example of MR image acquired using the SPGR sequence and the body coil before stabilizing the coil. The image quality was compromised by RF interference. This observation emphasized the importance of proper coil position and its effect on image quality.

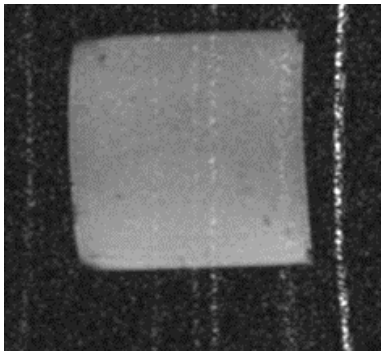

Figure 31. Example of a coronal image acquired with the body coil using a SPGR sequence and the transducer power set to 200 W, before changing the positioning of the body coil. Notice how image quality is compromised by RF interference.

GP FLEX coil

Figures 32, 33 and 34 show the images acquired using the SPGR sequence and the multi-purpose flex surface coil. Figure 32 shows images acquired at different activation states of the system, whereas Figures 33 and 34 show the images acquired at different acquisition times (with the power ON or OFF) using electric power of 100 and 200 W, respectively.

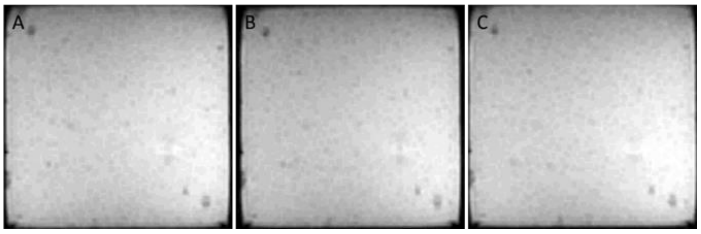

Figure 32. Coronal images acquired using the 2D SPGR sequence for various activation states: (A) Cables OFF, (B) Cables ON, and (C) Amplifier ON.

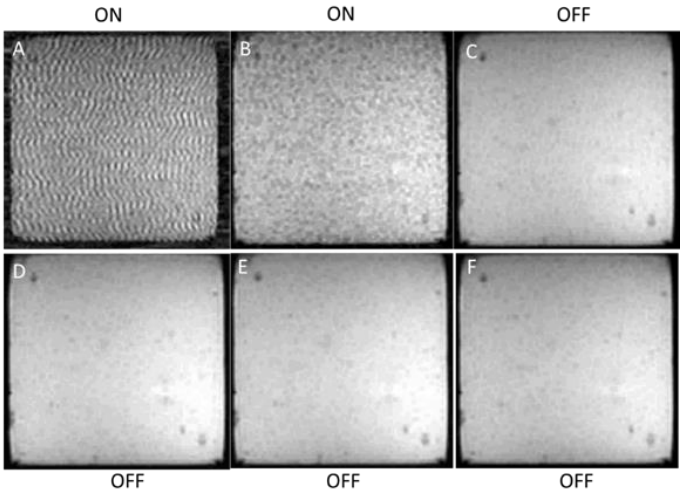

Figure 33. Coronal images acquired using the 2D SPGR sequence for different acquisition times. Power was set to 100 W (for 12 s) during the scan and the duration of the acquisition was 4s. Images were acquired at (A) 4 s, (B) 8 s, (C) 12 s, (D) 14 s, (E) 16 s, and (F) 20 s.

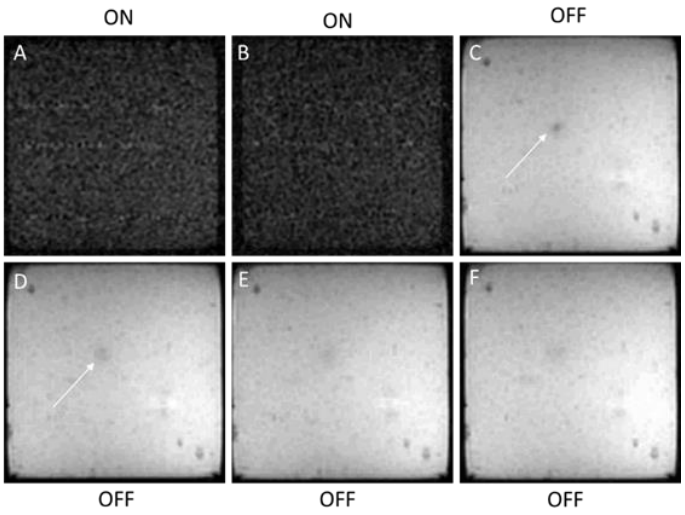

Figure 34. Coronal images acquired using the 2D SPGR sequence for different acquisition times. Power was set to 200 W (for 12 s) during the scan and the duration of the acquisition was 4s. Images were acquired at (A) 4 s, (B) 8 s, (C) 12 s, (D) 14 s, (E) 16 s, and (F) 20 s.

Figures 35, 36 and 37 show the corresponding images acquired using the T1W FSE sequence and the multi-purpose flex surface coil.

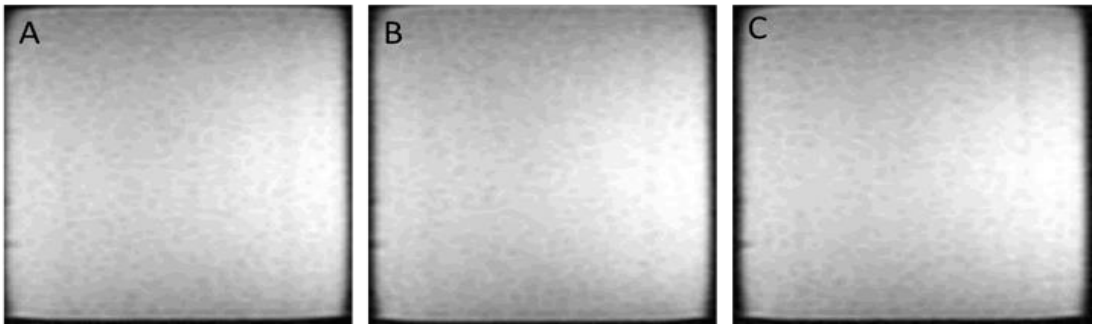

Figure 35. Coronal images acquired using the T1W FSE sequence for various activation states: (A) Cables OFF, (B) Cables ON, and (C) Amplifier ON.

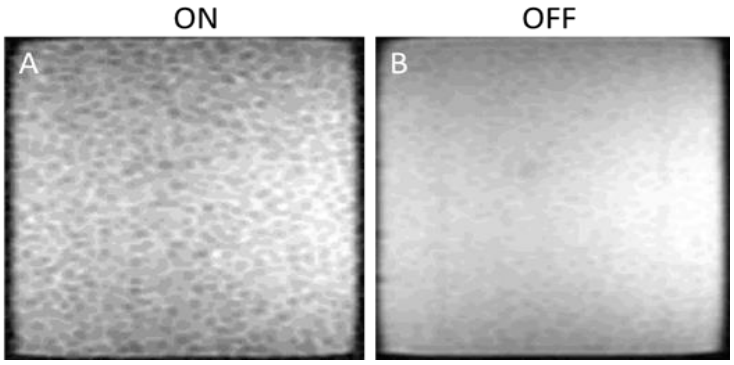

Figure 36. Coronal images acquired using the T1W FSE sequence for different acquisition times. Power was set to 100 W (for 13 s) during the scan and the duration of the acquisition was 13s. Images were acquired at (A) 13 s and (B) 26 s.

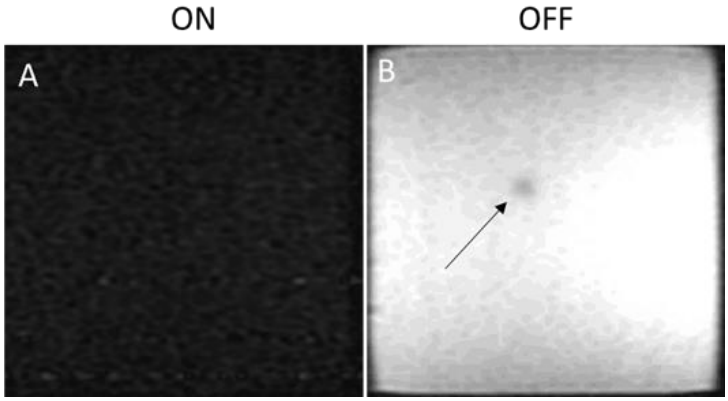

Figure 37. Coronal images acquired using the T1W FSE sequence for different acquisition times with the flex surface coil. Power was set to 200 W (for 13 s) during the scan and the scan time was 13 s. Images were acquired at (A) 13 s and (B) 26 s.

Body Coil

Figures 38, 39 and 40 show the images acquired using the SPGR sequence and the body coil. Figure 38 shows images acquired at different activation states of the system, whereas Figures 39 and 40 show the images acquired at different acquisition times (with the power ON or OFF).

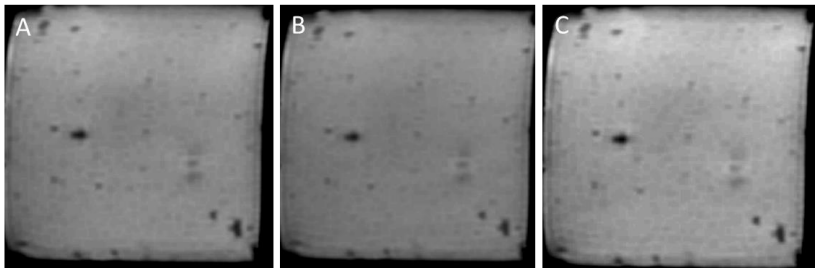

Figure 38. Coronal slice acquired using the 2D SPGR sequence for various activation states: (A) Cables OFF, (B) Cables ON, and (C) Amplifier ON.

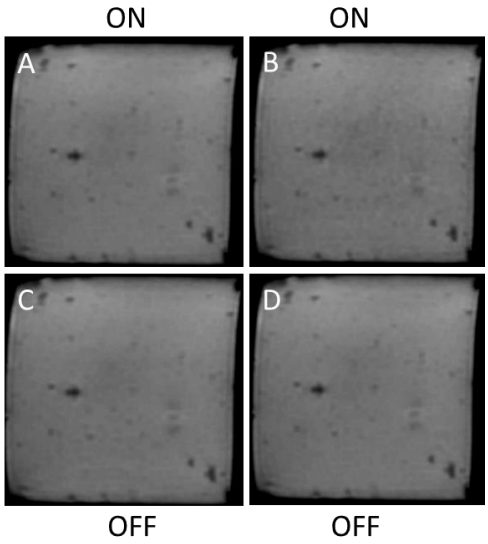

Figure 39. Coronal slice acquired using the 2D SPGR sequence for different acquisition times. Power was set to 100 W (for 10 s) during the scan and the duration of the acquisition was 5s. Images were acquired at (A) 5 s, (B) 10 s, (C) 15 s, and (D) 20 s.

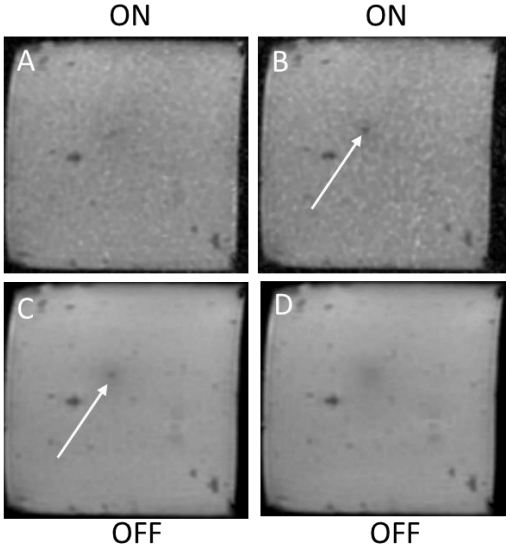

Figure 40. Coronal slice acquired using the 2D SPGR sequence for different acquisition times. Power was set to 100 W for 10 s during the scan and the duration of the acquisition was 5 s. Images were acquired at (A) 5 s, (B) 10 s, (C) 15 s, and (D) 20 s.

Figures 41, 42 and 43 show the corresponding images acquired using the T1W FSE sequence and the body coil.

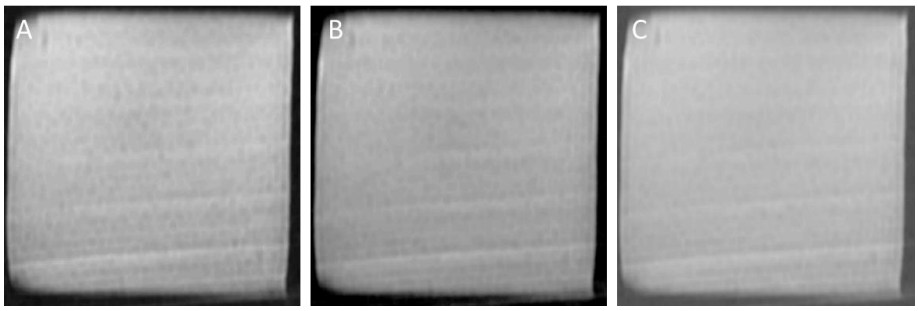

Figure 41. Coronal slice acquired using the T1W FSE sequence for various activation states: (A) Cables OFF, (B) Cables ON, and (C) Amplifier ON.

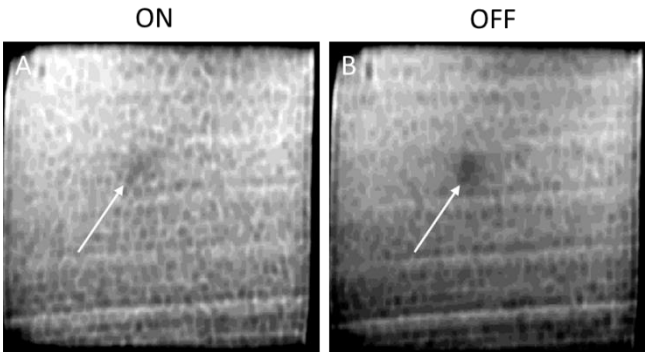

Figure 42. Coronal slice acquired using the T1W FSE sequence for different acquisition times. Power was set to 100W (for 13s) during the scan and the duration of the acquisition was 13 s. Images were acquired at (A) 13 s and (B) 26 s.

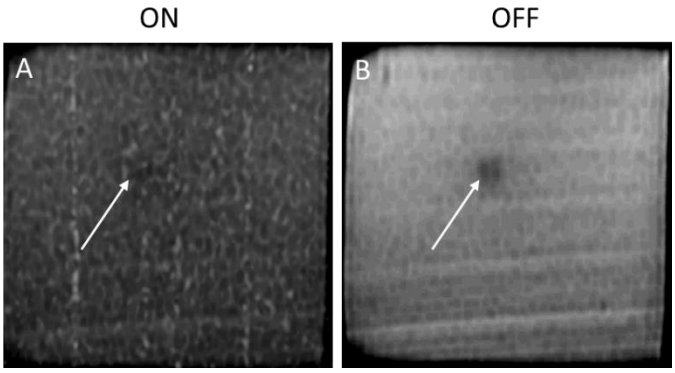

Figure 43. Coronal slice acquired using the T1W FSE sequence for different acquisition times. Power was set to 200 W (for 13 s) during the scan and the duration of the acquisition was 13s. Images were acquired at (A) 13 s and (B) 26 s.

SNR Measurements

Figures 44 and 45 show SNR measurements taken using SPGR and T1W FSE sequences for each coil (surface and body coils, respectively), for the following activation states: No Cables connected, Cable connected and Amplifier ON. There is no significant change in SNR for these states.

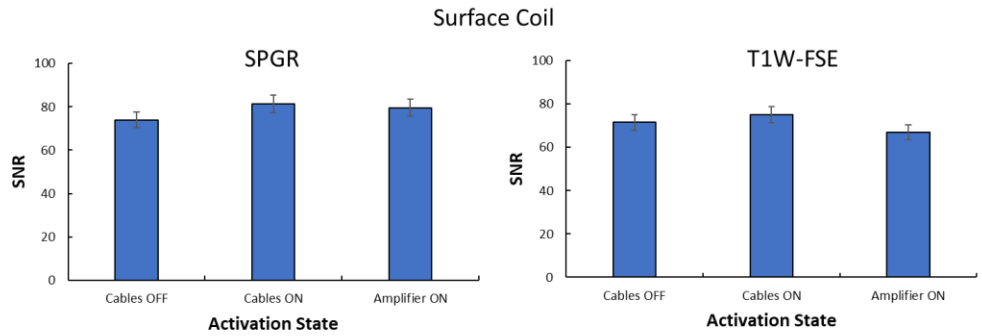

Figure 44. (Left) Bar chart of SNR (with error bars) for the different activation states using the surface coil and a SPGR sequence. (Right) Bar chart of SNR (with error bars) for the different activation states using the surface coil and a T1W FSE sequence.

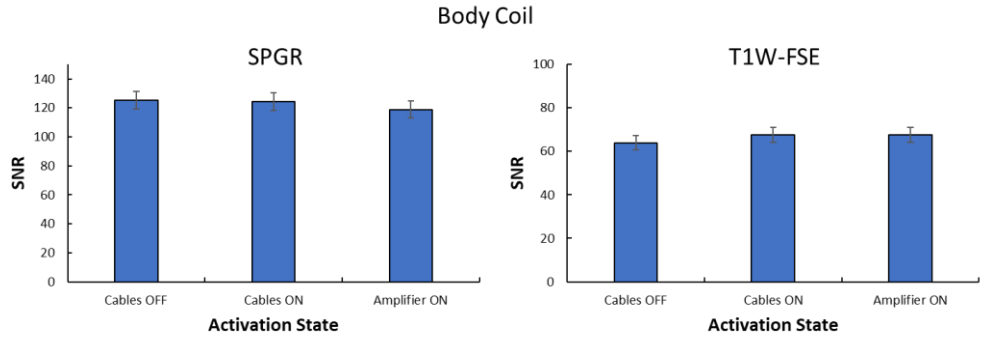

Figure 45. (Left) Bar chart of SNR (with error bars) for the different activation states using the body coil and a SPGR sequence. (Right) Bar chart of SNR (with error bars) for the different activation states using the body coil and a T1W FSE sequence.

Figures 46 and 47 show bar charts of the SNR measured using the SPGR and T1W FSE sequences, respectively, for different acquisition times with the transducer power ON or OFF, for both coils. The image acquisition was dynamic, i.e., images were acquired at a specific temporal resolution (as shown in Figures 46 and 47) while the power of the US transducer was set from ON state to OFF state.

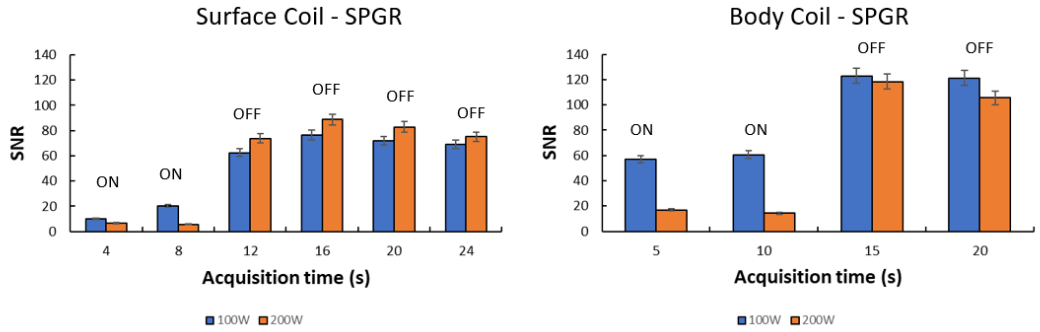

Figure 46. (Left) Bar chart of SNR (with error bars) for the different acquisition times using the surface coil and a SPGR sequence. (Right) Bar chart of SNR (with error bars) for the different acquisition times using the body coil and a SPGR sequence. Both power settings (100W and 200W) are displayed.

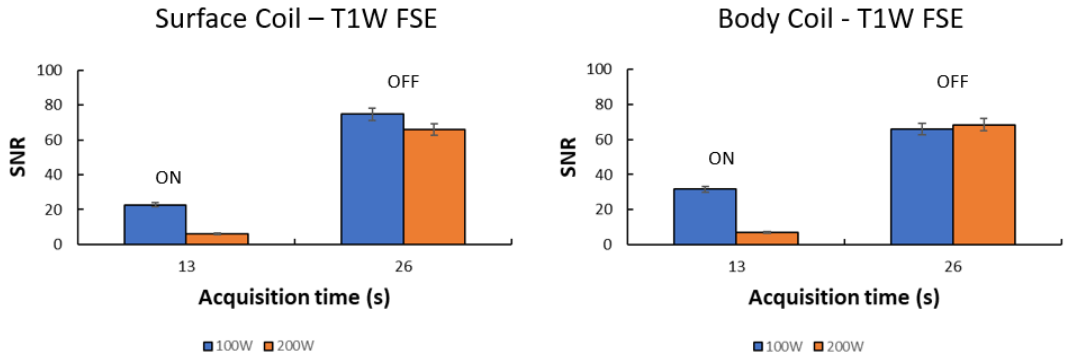

Figure 47. (Left) Bar chart of SNR (with error bars) for the different acquisition times using the surface coil and a T1W FSE sequence. (Right) Bar chart of SNR (with error bars) for the different acquisition times using the body coil and a T1W FSE sequence. Both power settings (100W and 200W) are displayed.

MR compatibility of the SOUNDPET Robotic System v3

The purpose of the following set of measurements was to assess the SNR and image quality at different activation states of the SOUNPET robotic system v3 (transducer and robotic device). The robotic device was placed on the MRI couch, as shown in Figure 48. An agar-based phantom (6 % w/v agar) was placed at the acoustic opening above the US transducer (ID: 57, diameter: 50mm, radius of curvature: 65mm, frequency: 2.453 MHz). To reduce image artifacts from vibrations of the phantom during sonication, the shape of the phantom was properly modified so that its bottom part was fitted in a holder (that was attached to the acoustic opening), thus providing extra stability (Figure 49). The US transducer was connected to the amplifier AG1016 (AG Series Amplifier, T & C Power Conversion, Inc., Rochester, US).

Figure 48. SOUNDPET Robot v3 positioned on the MRI table. An agar-based phantom was placed at the acoustic opening above the transducer. An orthogonal plastic positioner was used to properly position the body coil at sufficient distance above the phantom. (A) Cables disconnected, (B) Cables connected, and (C) Transducer Cable connected.

The phantom was scanned with the body coil using SPGR and FSE sequences (parameters listed in Table 11). To assess the effect of different activation states of the US transducer on the MR image, the following conditions were tested:

I. Reference image

II. Cables disconnected

III. Cables ON

IV. Amplifier ON

V. Power set to 50 W for 20 s

VI. Power set to 100 W for 20 s

VII. Power set to 150 W for 20 s

VII. Power set to 200 W for 20 s

To assess the effect of different activation states of the robotic device on the MR image, the following conditions were tested:

I. Reference image

II. Cables OFF

III. Cables ON

IV. DC ON

V. Motor moving

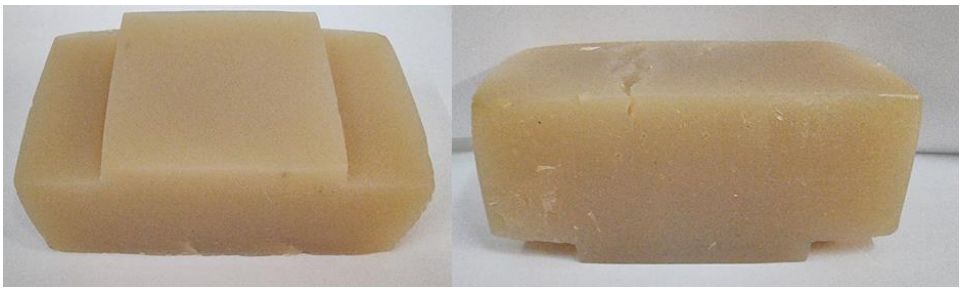

Figure 49. The agar-based phantom (6 % w/v agar) used in the experiment. Its shape was such as its top part was supported on the plastic holder and only its bottom part was submerged into water.

Table 11. Sequence and Parameters for MR Imaging.

Sequences	Type	Coil	Acquisition Type	TR (ms)	TE (ms)	TI (ms)	Flip Angle (degrees)	Echo Train Length	Pixel Bandwidth(Hertz/pixel)	Field of View (mm^3)	Acquisition Matrix Size(freq× phase)	No. of Averages	Acquisition Time/Slice (s)
T1W	FSE	Body	2D	300	6.94	-	90	3	75.11	280x280x10	128x128	0.5	9.2
2D SPGR	GE	Body	2D	22	8.4	-	30	1	62.96	280x280x10	192x160	2	7.1

Figure 50 and 51 show the images (FSE and SPGR, respectively) acquired during the various activation states of the transducer. Figures 52 and 53 show the results of the SNR analysis for the various activation states of the transducer (FSE and SPGR, respectively).

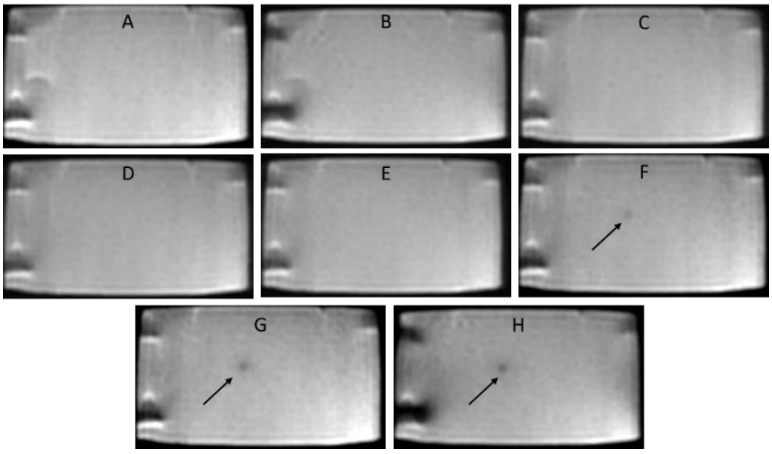

Figure 50. Coronal images acquired using the T1W FSE sequence and body coil for different activation states of the US transducer. (A) Reference image, (B) Cables disconnected, (C) Cables ON, (D) Amplifier ON, (E) Power set to 50W for 18s, (F) Power set to 100W for 20s, (G) Power set to 150W for 20s, and (H) Power set to 200W for 20s.

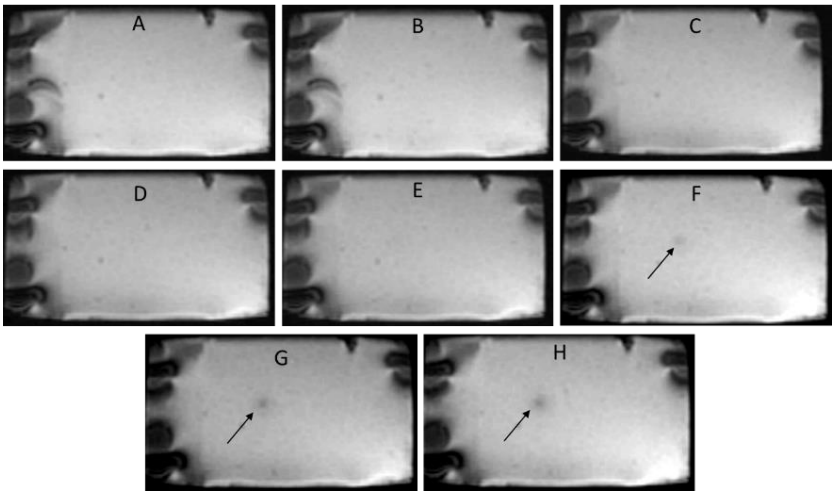

Figure 51. Coronal images acquired using the 2D SPGR sequence and body coil for different activation states of the US transducer. (A) Reference image, (B) Cables disconnected, (C) Cables ON, (D) Amplifier ON, (E) Power set to 50W for 16s, (F) Power set to 100W for 16s, (G) Power set to 150W for 16s, and (H) Power set to 200W for 16s.

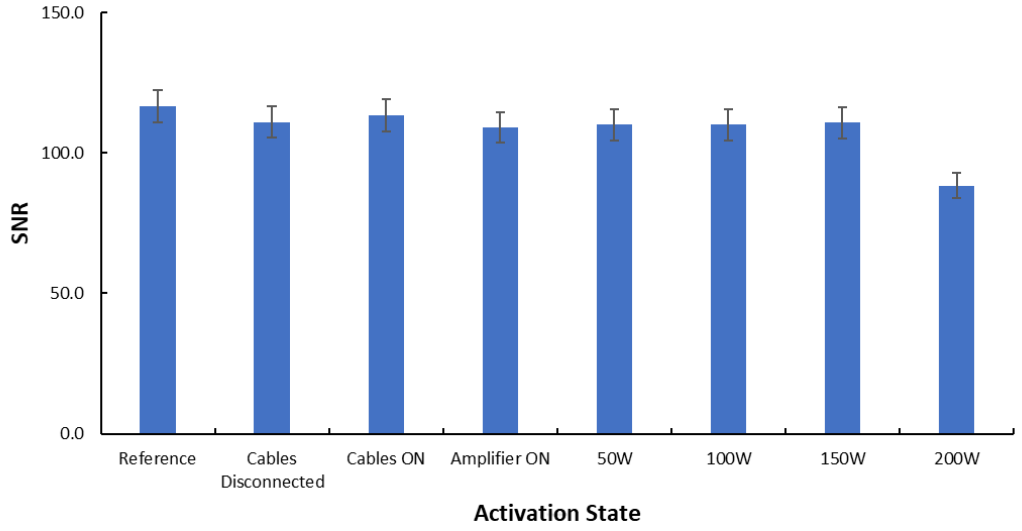

Figure 52. Bar chart of SNR (with error bars) for the different activation states of the US transducer using T1W FSE sequence.

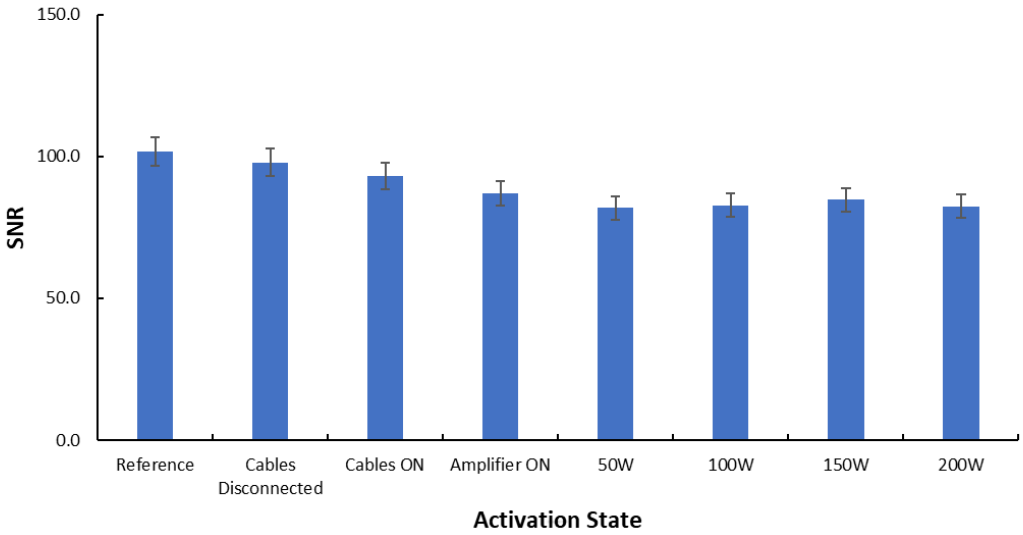

Figure 53. Bar chart of SNR (with error bars) for the different activation states of the US transducer using 2D SPGR sequence

Figures 54 and 55 show the images (FSE and SPGR, respectively) acquired during the various activation states of the robotic device. Figures 56 and 57 show the results of the SNR analysis for the various activation states of the robotic device (FSE and SPGR, respectively).

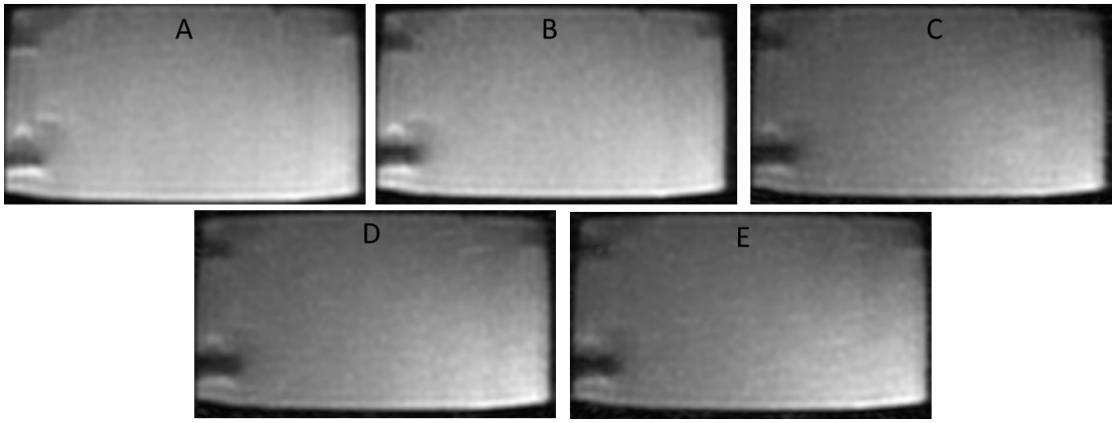

Figure 54. Coronal images acquired using the T1W FSE sequence and body coil for different activation states of the robotic device. (A) Reference image, (B) Cables disconnected, (C) Cables ON, (D) DC ON, and (E) Motor moving.

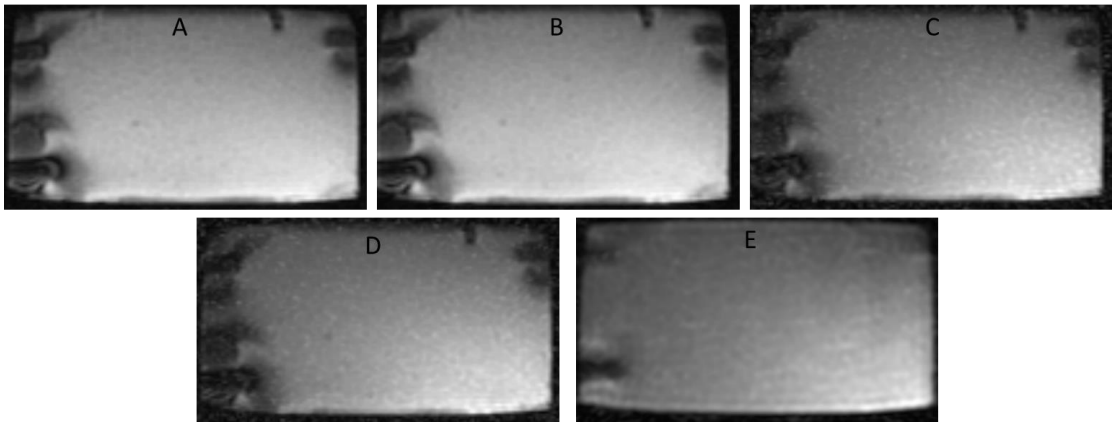

Figure 55. Coronal images acquired using the 2D SPGR sequence and body coil for different activation states of the robotic device. (A) Reference image, (B) Cables disconnected, (C) Cables ON, (D) DC ON, and (E) Motor moving.

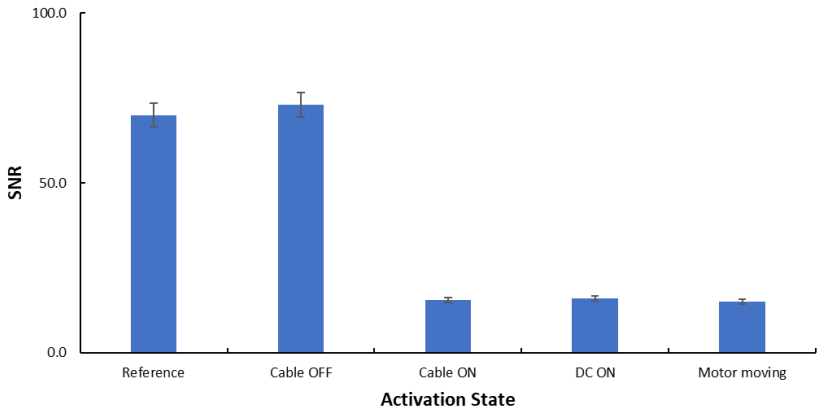

Figure 56. Bar chart of SNR (with error bars) for the different activation states of the robotic device using T1W FSE sequence.

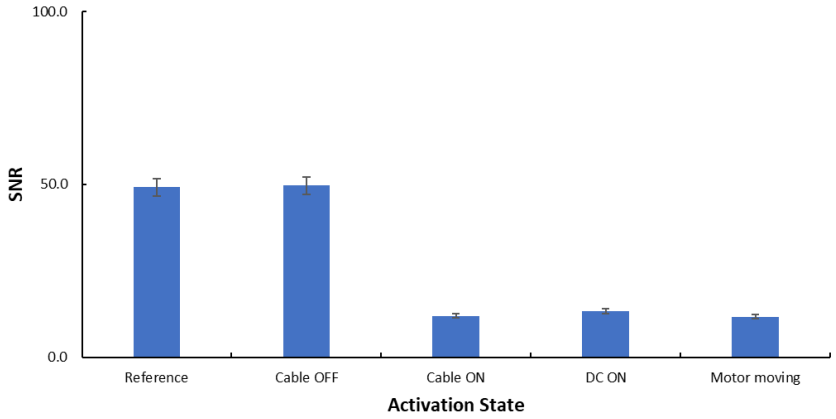

Figure 57. Bar chart of SNR (with error bars) for the different activation states of the robotic device using 2D SPGR sequence.

MR compatibility of the SOUNDPET Robotic System v3: Coil position testing

The purpose of this experiment was to assess the SNR and image quality at different activation states of the SOUNDPET Robot 3. A similar setup was used as described previously (Figure 48) using the phantom shown in Figure 49, but the body coil was moved away from the location of the motors to examine whether this has a positive impact on the background noise and image quality. For MR image acquisition, SPGR and FSE sequences were used. The specific parameters of each sequence are listed in Table 12.

Table 12. Sequence and Parameters for MR Imaging.

Sequences	Type	Coil	Acquisition Type	TR (ms)	TE (ms)	TI (ms)	Flip Angle (degrees)	Echo Train Length	Pixel Bandwidth (kHz)	Field of View (mm^3)	Acquisition Matrix Size(freq× phase)	No. of Averages	Acquisition Time/Slice (s)
T1W	FSE FS	Body	2D	300	6.94	-	90	3	9.6	280x280x10	128x128	0.5	9.2
2D SPGR	GE	Body	2D	22	10.5	-	30	1	8.9	280x280x10	192x160	2	7.1

To assess the effect of different activation states of the robotic device on the MR image, the following conditions were tested (for the SPGR sequence more activation states were tested, as shown in Figure 58):

I. Reference image – Cables connected

II. DC ON

III. Motor moving

IV. Cables disconnected

Figures 58 and 59 show the images acquired at different activation states of the robotic system v3 using SPGR and FSE sequences, respectively.

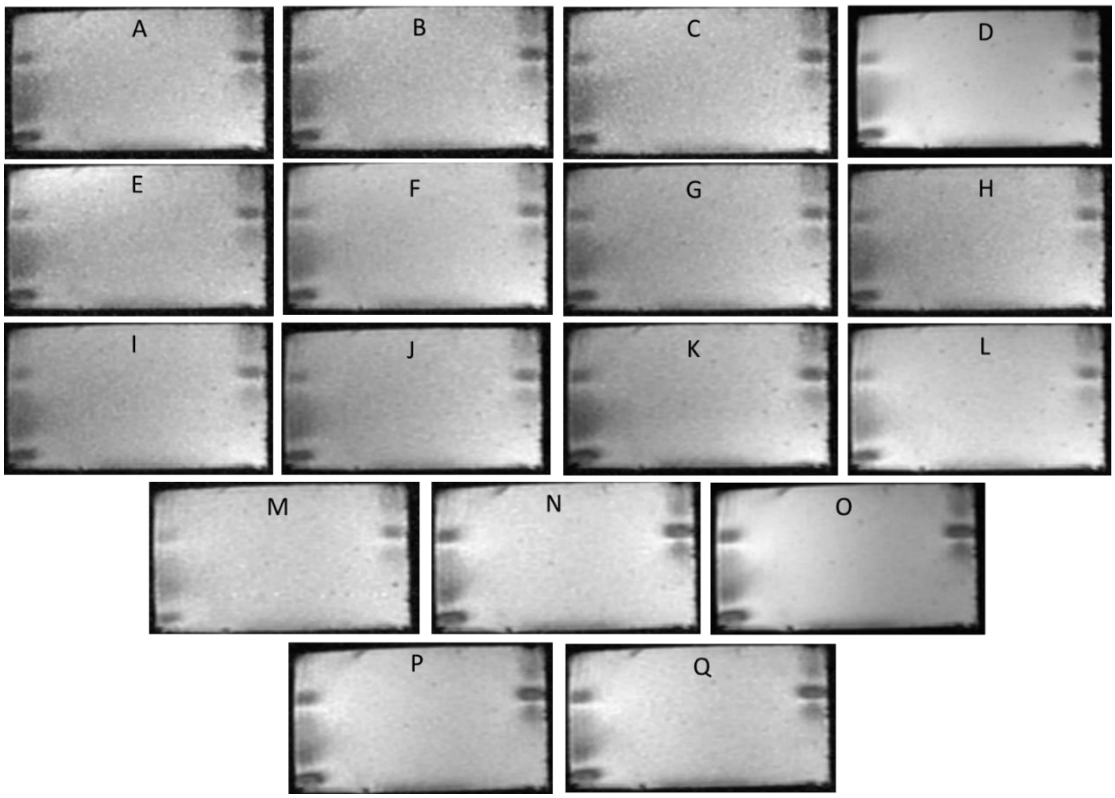

Figure 58. Coronal images acquired using 2D SPGR sequence and body coil for different activation states of the SOUNPET Robot v3: (A) Cables connected, (B) DC ON, (C) Motor moving, (D) Cables disconnected, (E) Cables connected – encoder cables separated and DC OFF, (F) Cables connected – cables kept off the floor and DC OFF, (G) Cables connected – stable position of the cables, (H) DC ON, (I) Motor moving, (J) DC ON - No. of Phase:128, (K) DC ON - BW 6 kHz, (L) Cables disconnected, (M) Cables connected – motors moved away from the coil, (N) Slice position placed at the centre of the phantom, (O) Cables disconnected, (P) Motor moving, and (Q) DC ON.

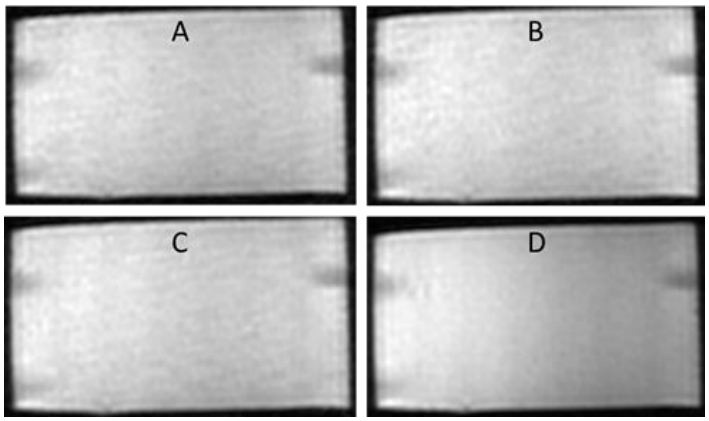

Figure 59. Coronal images acquired using T1W FSE sequence and body coil for different activation states of the SOUNPET Robot v3: (A) DC OFF, (B) DC ON, (c) Motor moving, and (D) Cables disconnected.

Figures 60 shows bar charts of the SNR calculation for the SPGR sequence for all activations states. Figure 61 shows a bar chart of the acquired SNR for those activation conditions where the DC was on. Accordingly, Figures 62 to 64 show the corresponding graphs for the activation conditions where a) the cables were connected, b) the motors were moving, and c) the cables were disconnected, respectively.

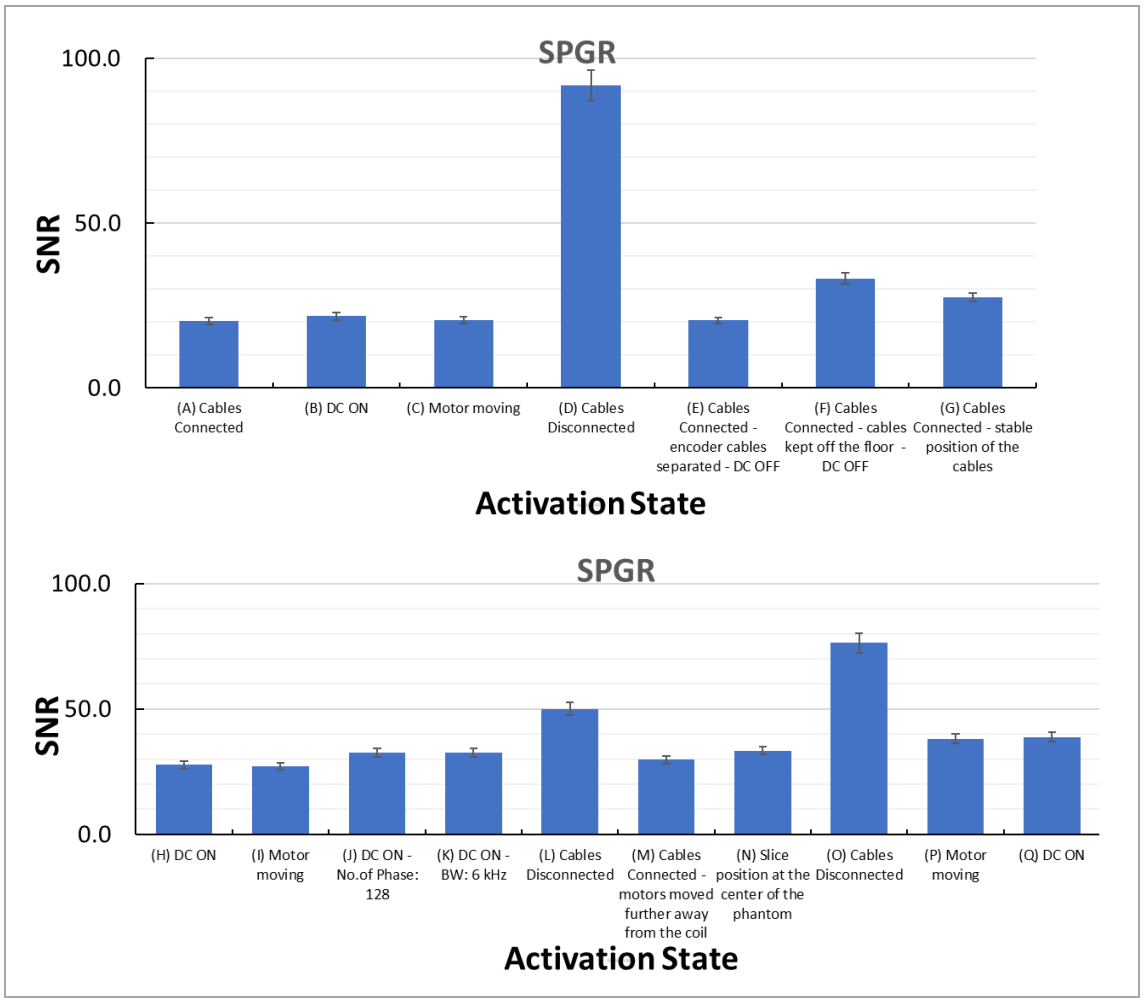

Figure 60. Bar chart of SNR (with error bars) for the different activation states of the robot v3 using 2D SPGR sequence.

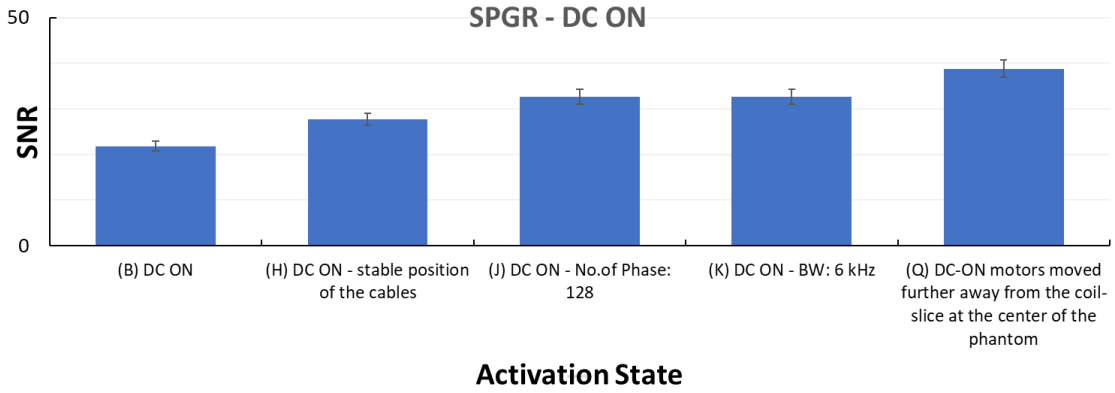

*Figure 61. Bar chart of SNR (with error bars) for the **different DC ON-states** of the robot v3 using 2D SPGR sequence.*

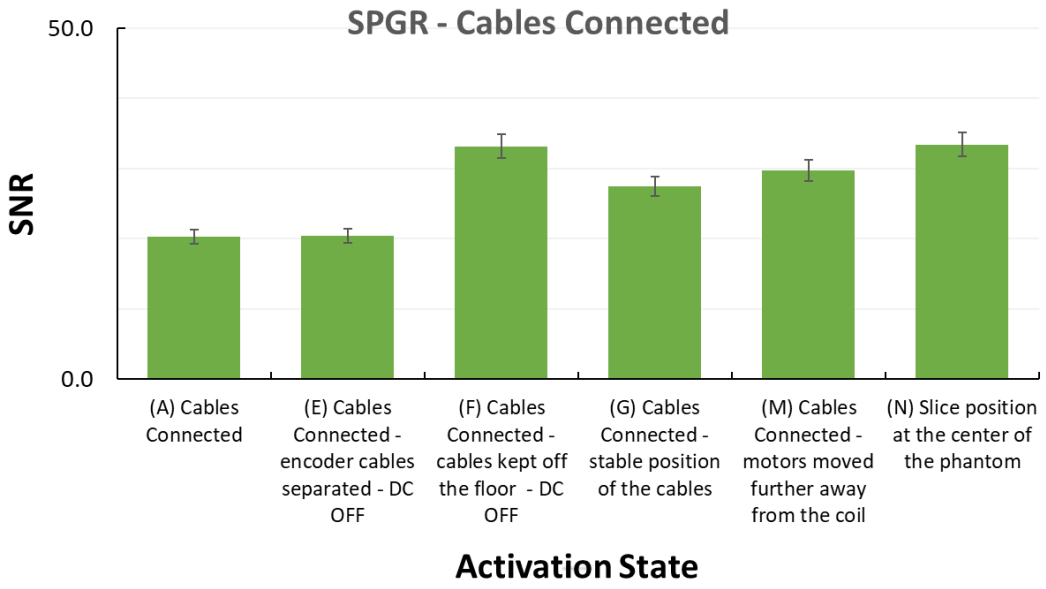

*Figure 62. Bar chart of SNR (with error bars) for the **different cables connected-states** of the robot v3 using 2D SPGR sequence.*

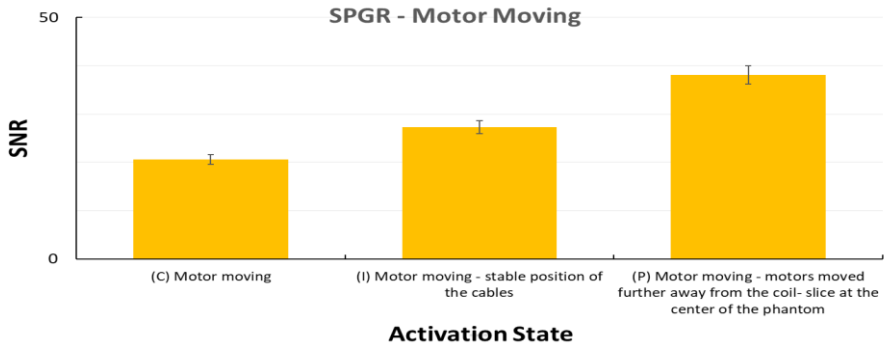

*Figure 63. Bar chart of SNR (with error bars) for the **different motor moving-states** of the robot v3 using 2D SPGR sequence.*

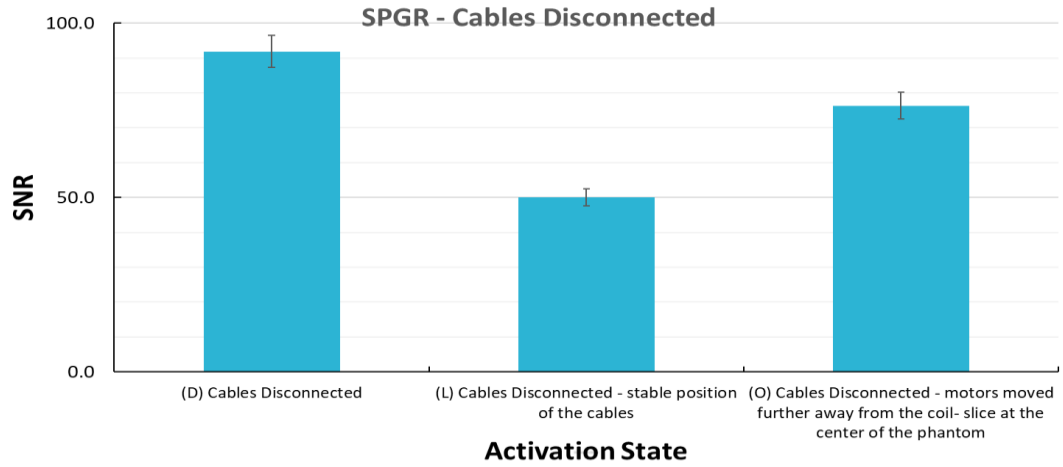

*Figure 64. Bar chart of SNR (with error bars) for the **different cable disconnected-states** of the robot v3 using 2D SPGR sequence.*

Figure 65 shows a bar chart of the SNR calculations for the FSE sequence. No calculations were performed for the EPI sequence because the image quality was poor.

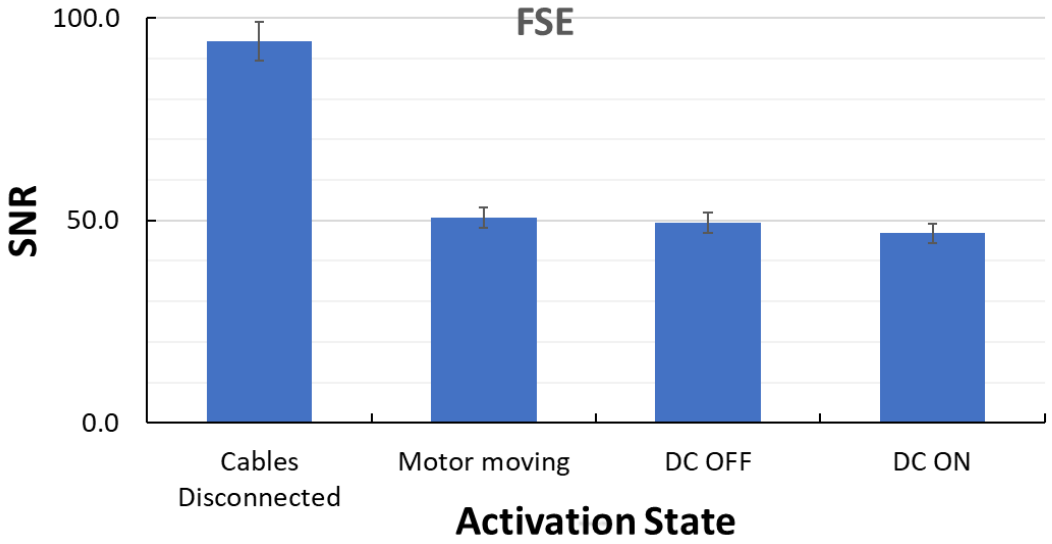

Figure 65. Bar chart of SNR (with error bars) for the different activation states of the robot v3 using T1W FSE sequence.

Conclusions

In this deliverable, the MR compatibility of three robotic systems was assessed under different activation states of the various components of the systems. MR images were acquired using FSE, EPI, and SPGR sequences. For the evaluation, we have used: a) visual assessment of the images, b) quantitative assessment through calculation of the SNR for the various activation conditions, and c) a more comprehensive approach of quality assurance using the ACR large phantom and a series of specialized tests.

The reproducibility experiments demonstrated that there is an inherent variability in the SNR due to random noise fluctuation even without changing any of the experimental conditions. This applied to all three sequences used. Hence, the drop in the SNR due to activation of a system's component should be sufficiently larger than the random SNR fluctuations observed in the reference images in order to conclude that system's activation affects the SNR significantly.

The MR compatibility assessment of the Robotic System v1 using T1W and T2W FSE fat suppressed images demonstrated that there were no visible differences in image quality when the cables were connected, and when the amplifier was ON compared to the reference image. However, the SNR calculation demonstrated that there was a small drop in SNR when the amplifier was ON, and a larger drop when the transducer was ON. The image quality was visibly compromised when the power was ON. This was also demonstrated by the large drop in SNR.

The MR compatibility of the Robotic System v1 was assessed using two different electronic driving systems. For this experiment, images were acquired using FSE, EPI

and FSPGR sequences under different activation states of the motors. Visual assessment of the acquired images indicates minimal impact on image quality. However, by examining the SNR there seems to be a drop in SNR when the motor is energized for both FSE and FSPGR sequences and both electronic systems. Using the EPI sequence, an increase in SNR was recorded when the motors were energized. However, this might be due to background fluctuations in the acquired images as suggested by the reproducibility experiments. It is important to note that the cables were fed to the robotic device through the penetration panel, which resulted in minimal SNR drop. This approach is far better than feeding the wires through the waveguide opening, which results in severe drop in SNR as shown in past experiments.

The MR compatibility of the Robotic System v2 was assessed using an electronic driving system designed to control larger motors. For both FSE and EPI sequences, the SNR measurements for all the activation states were significantly different compared to each other. This suggests that the variability of the image signal is high, whereas the signal does not seem to change dramatically after the motor is energized. In other words, despite that a small decrease in SNR was observed when the motor was energized compared to the reference image, the SNR looks similar to that recorded when only the cables were connected. On the other hand, the SNR calculated for the FSPGR sequence seems to significantly decrease when the motor driver is ON, the interface is connected, and the motor is energized. We have also tested whether the position of the coil with respect to the meat's position has an effect on image quality. The results suggest that when the coil is in proximity to the top of the meat, the image quality is reduced compared to when the coil is placed at a distance (i.e., not touching the meat). Furthermore, the results showed that as the power of the transducer is increased the SNR decreases.

The Robotic System v2 was also evaluated for MR compatibility according to the ACR MRI quality assurance guidelines. Images of a large ACR phantom were acquired to assess the robot's impact on MRI performance. The following tests have been performed: geometric accuracy, high contrast spatial resolution, slice thickness accuracy, slice position accuracy, image intensity uniformity, percent signal ghosting, and low contrast object detectability. The results from all tests were well within the permitted limits given by the ACR MRI Accreditation Program. These results suggest that the SOUNDPET Robotic System v2 is MR compatible when used under the conditions described in this experiment.

The MR compatibility of SOUNDPET Robotic System v2 was also tested using two different coils, the GP FLEX coil (single channel) and the body coil (12 channel). The SPGR sequence was used (instead of FSPGR) since it is also suitable for MR Thermometry. The results suggest that the SPGR sequence offers a higher SNR compared to the T1W FSE sequence, for both coil combinations. In agreement with previous experiments, there was no significant difference in SNR when the robot's activation state changed from 'no cables attached' to 'cables connected', and then to 'cables ON'. It was also proven that the image quality with the power on was significantly better when the coil was positioned at a distance from the transducer. Furthermore, it was proven that the coil selection has a major impact on image quality. The body coil, due to its higher number of channels and higher order shimming capabilities, offers a higher SNR and better image quality compared to the GP FLEX coil, when used under the same conditions. The coil selection should therefore be considered in future studies.

Finally, the MR compatibility of the SOUNDPET Robotic System v3 was assessed using a similar experimental setup as the one used for the other two versions. The measurements were made in two parts. In the first, the impact of different activations states of the US transducer on image quality was assessed, whereas the second part focused on the effect of the robotic device's activation on the image quality. Notably, for these experiments, the shape of the phantom was modified so as to fit in the acoustic opening of the water container, thus improving its stability during exposures. This modification significantly reduced the phantom's vibrations caused during sonications, and thus, greatly improved the SNR and image quality. No noticeable artifacts occurred compared to previous experiments, even at high power sonications.

Regarding MR compatibility assessment of the US transducer, for the MR parameters used for this experiment, the FSE sequence resulted in a higher SNR compared to SPGR. The focal heating spot was visible even for a 50 W power, using both sequences. However, this was not the case in the compatibility assessment of the robotic device itself. Both the image quality and SNR were significantly reduced when the cables were connected on the robotic device, irrespective of whether the DC power was ON or whether the motors were moving. To overcome this limitation, the body coil was moved further away from the location of the motors. This modification, in addition with the fact that the scanned slices were positioned at the isocenter, significantly improved the image quality and SNR when the cables were connected, compared to the previous setup (coil location overlapped with motor location). It should be noted that the benefits of this setup were tested using only FSE and SPGR sequences.

To summarize, the connection of cables to the SOUNDPET Robotic systems, as well as the activation of the amplifier and the transducer, do not significantly affect the SNR and the overall image quality of the MR phantom when FSE and EPI sequences are used. There is a decrease in SNR when the FSPGR sequence is used, even when the cables are just connected to the robotic systems. Furthermore, the SNR and image quality are affected when the connected motors are energized. However, this is a very extreme scenario (i.e., we don't expect to acquire images while the motors are energized). Therefore, imaging artefacts and SNR reduction due to this factor are not expected in practice. In the rare occasion where energization of the motors coincides with image acquisitions, the SNR and overall image quality could be improved significantly just by placing the imaging coil further away from the motors.

References

[1] Chinzei, K., Hata, N., Jolesz, FA., Kikinis, R. MR compatible surgical assist robot: system integration and preliminary feasibility study. In: Delp, SL., DiGoia, AM., Jaramaz, B., editors. MICCAI 2000. LNCS. Vol. vol. 1935. Springer: Heidelberg, 2000. P. 921-933.

[2] Gregory S. Fischer, Axel Krieger, Iulian Iordachita, Csaba Csoma, Louis L. Whitcomb, and Gabor Fichtinger. MRI Compatibility of Robot Actuation Techniques-A Comparative Study. Med Image Comput Comput Assist Interv. 2008; 11 (Pt 2): 509-517.

[3] L. Bendel. The effect of mechanical deformation on magnetic properties of MRI artifacts of type 304 and 316L stainless steel. J. Magn. Reason. Imaging 7, 1190-1173 (1997).

[4] Damianou C, Giannakou M, Yiallouras C, Menikou G. The role of three-dimensional printing in magnetic resonance imaging-guided focused ultrasound surgery. Digit Med 2018; 4: 22-6.

[5] R. Chopra, L. Curiel, R. Staruch, L. Morrison, and K. Hynynen. An MRI-compatible system for focused ultrasound experiments in small animal models. Med. Phys. 36, 1867-1874 (2009).

[6] C. Yiallouras and C. Damianou. Review of MRI positioning devices for guiding focused ultrasound systems. Int. J. Med. Rob. Comput. Assisted Surg. 11, 247-255 (2015).

[7] FDA. Establishing safety and compatibility of passive implants in the magnetic resonance (MR) environment. Technical Report, Food and Drug Administration, 2014.

[8] ASTM. Standard practice for marking medical devices and other items for safety in the magnetic resonance environment. Technical Report ASTM F2503-13, ASTM International, West Conshohocken, PA, 2013.

[9] T. Mashimo and S. Toyama. MRI-Compatibility of a Manipulator using a Spherical Ultrasonic Motor. 12th IFToMM World Congress, Besancon (France), June 18-21, 2007.

[10] Axel Krieger, Sang-Eun Song, Nathal B. Cho, Iulian Iordachita, Peter Guion, Gabor Fichtinger, and Louis L. Whitcomb. Development and Evaluation of an Actuated MRI-Compatible Robotic System for MRI-Guided Prostate Intervention. IEEE ASME Trans Mechatron, 2012 September 12; 18(1): 273-284.

[11] Haytham Elhawary, Aleksander Zivanovic, Marc Rea, Brian Davies, Collin Besant, Donald McRobbie, Nandita de Souza, Ian Young, and Michael Lamperth. The Feasibility of MR-Image Guided Prostate Biopsy Using Piezoceramic Motors Inside or Near to the Magnet Isocentre. MICCAI 2006, LNCS 4190, pp. 519-526.

[12] Yi Wang, Gregory A. Cole, Hao Su, Julie G. Pilitsis and Gregory S. Fischer. MRI Compatibility Evaluation of a Piezoelectric Actuator System for a Neural Interventional Robot. 31st Annual International Conference of the IEEE EMBS, 2009.

[13] Roger Gassert, Akio Yamamoto, Dominique Chapuis, Ludovic Dovat, Hannes Bleuler, and Etienne Burdet. Actuation Methods for Applications in MR Environments. Magnetic Resonance Engineering, 2006, Vol 29B(4): 191-209.

[14] Li-Wei Kuo, Li-Chen Chiu, Win-Li Lin, Jiun-Jung Chen, Guo-Chung Dong, Sheng-Fu Chen, and Gin-Shin Chen. Development of an MRI-Compatible High-Intensity Focused Ultrasound Phased Array Transducer Dedicated for Breast Tumor Treatment. IEEE Transactions on Ultrasonics, Ferroelectrics, and Frequency Control, vol., 65, No. 8, 2018.

[15] Takashi Azuma, Kazuaki Sasaki, Ken-ichi Kawabata, Akiko Osada, Hiroyuki Itagaki, Kazumi Komura, Tetsuhiko Takahashi, Kazunari Ishida, Yutaka Satoh and Shin-ichiro Umemura. MRI-Compatible ultrasonic probe for minimally invasive therapy. IEEE Ultrasonics Symposium, 1465, 2002.